TURBULENT COMPRESSIBLE CONVECTION WITH ROTATION. I. FLOW STRUCTURE AND EVOLUTION

NICHOLAS H. BRUMMELL
JILA and Department of Astrophysical, Planetary and Atmospheric Sciences, University of Colorado, Boulder, CO 80309-0440

NEAL E. HURLBURT
Lockheed Martin Solar and Astrophysics Laboratory, Org. 91-30, Building 252, 3251 Hanover Street, Palo Alto, CA 94304

AND

JURI TOOMRE
JILA and Department of Astrophysical, Planetary and Atmospheric Sciences, University of Colorado, Boulder, CO 80309-0440

ABSTRACT

The effects of Coriolis forces on compressible convection are studied using three-dimensional numerical simulations carried out within a local modified f-plane model. The physics is simplified by considering a perfect gas occupying a rectilinear domain placed tangentially to a rotating sphere at various latitudes, through which a destabilizing heat flux is driven. The resulting convection is considered for a range of Rayleigh, Taylor, and Prandtl (and thus Rossby) numbers, evaluating conditions where the influence of rotation is both weak and strong. Given the computational demands of these high-resolution simulations, the parameter space is explored sparsely to ascertain the differences between laminar and turbulent rotating convection. The first paper in this series examines the effects of rotation on the flow structure within the convection, its evolution, and some consequences for mixing. Subsequent papers consider the large-scale mean shear flows that are generated by the convection, and the effects of rotation on the convective energetics and transport properties.

It is found here that the structure of rotating turbulent convection is similar to earlier nonrotating studies, with a laminar, cellular surface network disguising a fully turbulent interior punctuated by vertically coherent structures. However, the temporal signature of the surface flows is modified by inertial motions to yield new cellular evolution patterns and an overall increase in the mobility of the network. The turbulent convection contains vortex tubes of many scales, including large-scale coherent structures spanning the full vertical extent of the domain involving multiple density scale heights. Remarkably, such structures align with the rotation vector via the influence of Coriolis forces on turbulent motions, in contrast with the zonal tilting of streamlines found in laminar flows. Such novel turbulent mechanisms alter the correlations which drive mean shearing flows and affect the convective transport properties. In contrast to this large-scale anisotropy, small-scale vortex tubes at greater depths are randomly orientated by the rotational mixing of momentum, leading to an increased degree of isotropy on the medium to small scales of motion there. Rotation also influences the thermodynamic mixing properties of the convection. In particular, interaction of the larger coherent vortices causes a loss of correlation between the vertical velocity and the temperature leaving a mean stratification which is not isentropic.

Subject headings: convection — hydrodynamics — stars: interiors — Sun: rotation — turbulence

1. INTRODUCTION

The dynamics within the outer envelope of late-type stars such as the Sun must control much of the observable activity at the stellar surface and in its extended atmosphere. Vigorous thermal convection serves to organize and transport energy, angular momentum, and magnetic fields within that envelope. Theoretical modeling of such stellar convection zones suffers from the complexity of the problem: the motions are compressible, almost certainly turbulent, supersonic in places, and are influenced by rotation, magnetic fields, changes in the equation of state and opacities due to ionization, and radiative transfer effects near the surface. Although simple linear and mixing-length models have contributed substantially to developing our physical intuition about convection (e.g., Busse 1970; Baker & Spiegel 1975; Gough & Weiss 1976; Rosner & Weiss 1985; Hathaway 1984; Durney 1987; Rüdiger 1989), many of the recent advances in stellar convection theory have come from numerical simulations, represented by three complementary thrusts. First, the desire to understand the coupling of rotation and convection has spawned work within full spherical shells. Such global models capture the correct geometry but are then restricted in their spatial resolution due to the limited computational resources (e.g., Gilman 1975, 1977; Busse & Cuong 1977; Gilman & Glatzmaier 1981; Glatzmaier & Gilman 1981; Glatzmaier 1984, 1985, 1987; Gilman & Miller 1986; Glatzmaier & Toomre 1995). Local models restrict the domain to small subsets of the global shell and can thus channel the finite computational degrees of freedom into resolving a greater spectrum of turbulent motions. One such approach includes much of the detailed physics of realistic gases and of radiative transfer in order to study the solar granulation scales by analyzing a region of modest horizontal extent and of a limited interval in depth close to the solar surface (e.g., Nordlund 1982, 1983, 1984, 1985; Nordlund & Stein 1990, 1991; Stein & Nordlund 1991, 1994; Stein, Nordlund, & Kuhn 1989; Rast et al. 1993). More idealized approaches have simplified the physics by considering compressible convection in simple local domains containing perfect gases (e.g., Graham 1975,

1977; Sofia & Chan 1984; Latour, Toomre, & Zahn 1981; Massaguer et al. 1984; Chan & Sofia 1986, 1987; Hurlburt, Toomre, & Massaguer 1984, 1986; Cattaneo, Hurlburt, & Toomre 1989, 1990; Malagoli, Cattaneo, & Brummell 1990; Edwards 1990; Hossain & Mullan 1990; Porter et al. 1990; Toomre et al. 1990; Cattaneo et al. 1991; Brummell et al. 1991; Rast & Toomre 1993a, 1993b; Bogdan, Cattaneo, & Malagoli 1994; Porter & Woodward 1994; Hurlburt et al. 1994; Toomre & Brummell 1995). These models typically deal with planar convectively unstable layers bounded above and below by impenetrable planes or regions of stable stratification. Simulations of this type seek the generic properties of compressible convection, anticipating that these may provide insight into turbulence achieved within stars.

When taking the latter idealized approach toward stellar convection, the various physical processes must be prioritized for inclusion in the reduced model (cf. Brummell, Cattaneo, & Toomre 1995). Of basic importance is that the density contrast across a convection zone is generally large, and therefore the compressibility of the gas and the associated stratification must be taken into account. It has been shown that near the upper reaches of a convection zone in a stellar envelope, the resulting fast convective flows involve pressure and density fluctuations that may be comparable to their horizontal mean values (Hurlburt, Toomre, & Massaguer 1984; Stein & Nordlund 1989), and some flows may become intermittently supersonic (Woodward et al. 1987; Stein, Nordlund, & Kuhn 1989; Malagoli et al. 1990; Porter & Woodward 1994). Further, the fluid properties of the gases in typical convection zones are such that the scales of viscous dissipation are much smaller than those of thermal dissipation (i.e., the Prandtl number is very small), and the forcing is sufficiently nonlinear that Reynolds numbers R_e for the convective motions (on even the smallest scales) is extremely large. A typical order of magnitude estimate for R_e within the solar convection zone suggests values of 10^{12} or greater. This implies that the flows are highly turbulent in nature. Models including some degree of compressibility have existed for some time and have either been based on anelastic equations which filter out sound waves, or on the fully compressible Navier-Stokes equations. Attempting to compute flows in a fully turbulent regime is the more demanding aspect. The number of degrees of freedom needed to represent a flow is proportional to $R_e^{9/4}$, and thus even with present computational technology, the maximum resolvable Reynolds numbers remain of order 10^5. Such computations involving spatial resolution up to 1024^3 are sufficient for the flow to be intensely turbulent but still remain many orders of magnitude removed from physical reality within most stellar applications. As seen recently in both laboratory and numerical experiments studying incompressible Rayleigh-Benard convection (e.g., Heslot, Castaing, & Libchaber 1987; Castaing et al. 1989; DeLuca et al. 1990; Werne et al. 1991; Werne 1993), different regimes of turbulence (soft and hard) exist at high R_e in which the scaling of the heat transport and statistical properties of the flows change subtly, denying simple extrapolation of turbulent results from those at lower R_e values to far higher ones. Some notes of caution are therefore provided as one attempts to assess properties of stellar convection from the simulations of turbulent compressible flows currently feasible.

Numerical investigations of compressible convection in simple domains have only recently advanced from the laminar regime into the moderately turbulent regime, yet such excursions have already produced some unexpected results. Cattaneo et al. (1991) studied the transition to turbulence by reducing the effect of viscosity, thus increasing the Rayleigh and Reynolds numbers. They found that the topology of convection changed at low Prandtl numbers, with the majority of the domain in the vertical consisting of small-scale turbulent motions, accompanied by a surface layer laminarized into a smoothly evolving granulation-like network by the effects of small density scale heights there. Coherent strong downflows span the full extent of the turbulent interior, but contribute remarkably little to the horizontally-averaged transport of energy: the downward-directed flux of kinetic energy nearly counteracts the upward-directed enthalpy flux within the coherent structures. The dominant transport is left to the small-scale turbulent motions in a manner seemingly in accord with mixing-length theory. It was this surprising difference in the transport properties between turbulent and laminar compressible convection that led to the current study of how angular momentum transport within rotating stars may be influenced by this transition, in an attempt to understand the solar differential rotation profile.

Most stellar observations cannot probe deep below the surface of a star. Helioseismology, the observation of the acoustic p-mode oscillations of the Sun (for a review, cf. Gough & Toomre 1991), however, has provided some insight into flows within the interior, and the subject is likely to advance rapidly with new observations now becoming available from the Global Oscillations Network Group (GONG) project (e.g., Harvey et al. 1995) and from the Michelson Doppler Imager (SOI-MDI) instrument on the Solar Heliospheric Observatory (SOHO) spacecraft (e.g., Scherrer et al. 1995). Inversions of frequency splittings from the acoustic data have yielded estimates of the depth of the convection zone and have provided measures of the zonal angular velocity distribution with latitude and depth, known as the differential rotation profile. Such inferences about the rotation profile appear to be at striking variance with the predictions of earlier global-scale numerical convection models. The rotation profiles as deduced from helioseismic inversions (e.g., Brown & Morrow 1987; Libbrecht 1989; Brown et al. 1989; Gough & Toomre 1991; Tomczyk, Schou, & Thompson 1995; Korzennik et al. 1995) exhibit an angular velocity that at high latitudes appears to increase with depth, at midlatitudes is nearly constant on radial lines, and near the equator first increases and then gently decreases with depth within the convection zone. Spherical shell global simulations (e.g., Glatzmaier & Gilman 1981; Gilman & Miller 1986; Glatzmaier 1987) suggest that the largest scale motions in the convection zone are dominated by columnar roll-like cells orientated in the north-south direction, in a manner akin to what may be suggested by the Taylor-Proudman theorem (Proudman 1916; Taylor 1921). The shearing and tilting of these "banana cells" with latitude and depth provide correlations that lead to an angular velocity distribution which is nearly constant along the axes of the cells, and thus nearly constant on cylinders aligned with the rotation axis, and decreasing with depth in the equatorial plane. Hence there is an apparent disparity, with the helioseismic observations suggesting that angular velocity is roughly constant along radial lines, whereas the global simulations predict that

angular velocity is constant along cylinders parallel to the rotation axis.

A possible cause of this dilemma is that the spherical shell global simulations cannot achieve sufficient spatial resolution to describe highly turbulent motions within the convection zone. Computational constraints restricted the early global models to laminar or at most mildly turbulent flows, although new efforts are under way now using parallel computers to attain more turbulent flow regimes in global shells (Glatzmaier & Toomre 1995). Fully developed turbulence may transport and thus redistribute angular momentum in an very different manner, with consequences for the differential rotation profile. Whether the large-scale cells survive under more nonlinear conditions, or are replaced by other coherent structures through self-organization processes (inverse cascades) often seen in highly turbulent flows, is fundamentally unclear. Similarly, the dynamical effects of the intense small-scale convection near the solar surface on the far larger cells have not been determined with any confidence. Understanding such issues requires far more advanced models of compressible turbulent convection constrained by rotation. Clearly, even with current computational resources there are still major challenges getting adequate spatial resolution into global models, and thus it is necessary to turn to local models dealing with smaller horizontal segments of spherical shells.

The current series of papers describe the results from such a local model of compressible convection constrained by rotation. The scenario is essentially that of Cattaneo et al. (1991): a three-dimensional, rectilinear domain, periodic in the two horizontal dimensions but constrained by stress-free boundaries in the vertical, containing fully compressible, ideal gas, is subject to a heat flux at the lower boundary (and cooled to a constant temperature at the top) such that it convects vigorously. The primary modification is that f-plane rotation has been included in the equations, whereby a constant rotation vector generates Coriolis forces within the domain. The rotation vector lies in one vertical plane of the box (corresponding to the north-south vertical plane), but the angle between the rotation vector and gravity can be changed. Then the rotation vector has both vertical and horizontal components, and the local domain is effectively positioned at various latitudes on the true sphere. The basic physics here is highly simplified, presently omitting the effects of magnetic fields, ionization, and radiative transfer, but within such a local treatment the numerical resolution is sufficient that the thermal forcing and viscosity can be varied such that convection in substantially turbulent regimes can be examined. The strength of the rotation can be then be altered to study the effect of moderate to strong Coriolis forces on the turbulence and the consequences for the generation and distribution of large-scale mean flows. Such zonal shearing motions in the local model are related to differential rotation in the full spherical shell. Similar local f-plane models have been used to study the effect of rotation on laminar incompressible (Boussinesq) convection (e.g., Somerville & Lipps 1973; Hathaway & Somerville 1983, 1986, 1987; Hathaway 1984) and are currently employed by Julien et al. (1996) in the turbulent version of that problem. Pulkinnen et al. (1993) have also used a compressible version in the weakly nonlinear regime for comparison with mixing-length models (e.g., Rüdiger 1989).

This paper describes the model in some detail in § 2, and then in § 3 presents results bearing on the structure, evolution and mixing properties of turbulent convection when subject to rotational constraints. The subsequent papers will examine the generation of large-scale mean shearing flows relevant to differential rotation (Brummell, Hurlburt, & Toomre 1996, hereafter Paper II) and the energetics of such rotating flows.

2. FORMULATION

The physical model and pseudospectral numerical algorithms employed here are essentially those used by Cattaneo et al. 1991 for three-dimensional simulations of compressible convection. However, the effects of Coriolis forces are introduced using a modification of the rotating f-plane formulation, and the emphasis of the paper is on parameter ranges where fully turbulent convection is achieved.

2.1. *Physical Model*

Rotational effects are incorporated into the treatment of compressible convection using a "local modified f-plane model." A rectilinear domain placed tangentially to the sphere at a latitude ϕ is considered, as shown in Figure 1. Adopting a Cartesian coordinate system with x increasing to the east, y increasing to the north and z increasing with depth (downward), it is assumed that the rotational vector Ω has components which depend solely on the uniform angular velocity Ω_0 of the sphere and the mean latitude ϕ, namely

$$\Omega = (\Omega_x, \Omega_y, \Omega_z) = (0, \Omega_0 \cos \phi, -\Omega_0 \sin \phi) . \quad (1)$$

We call this formulation a local f-plane model because of the similarities between the assumptions of this method and those of the f-plane models of geophysical fluid dynamics (GFD) (see Pedlosky 1979). That is, it is assumed that the domain is small enough in latitudinal extent that the rotation vector is everywhere equal to its value at the mean latitude and that the layer is sufficiently shallow compared to the spherical radius that the domain may be considered flat. However, this model deviates from the typical GFD f-plane formulation in that it includes the horizontal component of the Coriolis force rather than assuming that the vertical component $f = 2\Omega_0 \sin \phi$ dominates. Keeping Ω constant throughout the domain permits computationally convenient periodic boundary conditions in the x and y directions. Subsequent simulations will deal with larger latitudinal extents, either allowing a linear variation of the Coriolis force in the y direction still in a flat geometry, akin to the GFD β-plane, or solving the equations in a segment of a curved shell in spherical coordinates (Hurlburt, Brummell, & Toomre 1995). These other formulations admit Rossby waves, and since these waves propagate only in the longitudinal direction, their coupling with the convective turbulence could lead to different statistics in the resulting meridional and zonal dynamics, including the associated mean flows.

The physics here is simplified as much as possible in order to elucidate the dynamical effects of compressibility and rotation on the turbulent convection. A plane-parallel layer of perfect gas is considered, confined in the vertical by two impenetrable, stress-free horizontal planes a distance d apart. The fluid is stratified under the action of a constant gravitational acceleration g, and it is assumed that the fluid possesses constant specific heats c_p and c_v, shear viscosity μ,
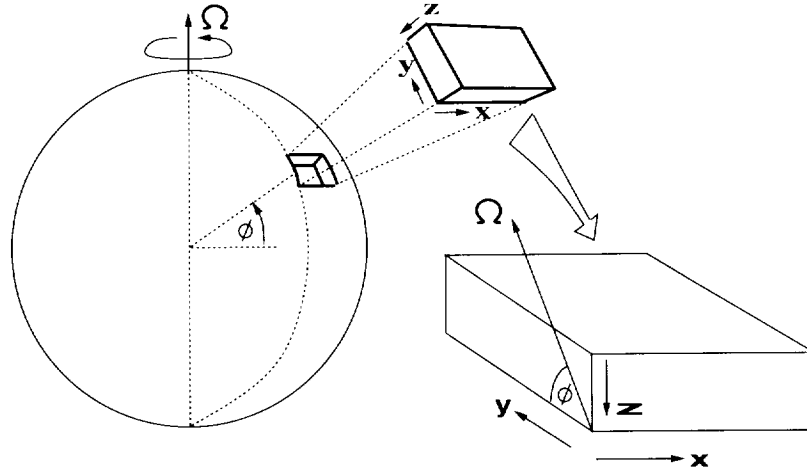
FIG. 1.—Local f-plane model positioned at latitude ϕ used to study flows in a portion of a spherical shell rotating with angular velocity Ω_0. The rectilinear coordinate system has the horizontal variables x increasing eastward and y poleward, the depth z increasing downward; the tilted rotation vector Ω thus lies in the $y - z$ plane.

and thermal conductivity K. A constant temperature T_0 is imposed on the upper boundary, and a constant temperature gradient Δ is enforced on the lower one. In the absence of motions, the above conditions are consistent with a polytropic solution to the equation of hydrostatic balance. If we take T_p, ρ_p, and p_p in turn as the temperature, density, and pressure in the polytropic state, then

$$T_p/T_0 = (1 + \theta \tilde{z}/d) , \tag{2a}$$

$$\rho_p/\rho_0 = (1 + \theta \tilde{z}/d)^m , \tag{2b}$$

$$p_p/p_0 = (1 + \theta \tilde{z}/d)^{m+1} , \tag{2c}$$

where ρ_0 is the density at the upper boundary, $p_0 = (c_p - c_v)T_0 \rho_0$, and $0 \leq \tilde{z} \leq d$. Here $m = -1 + g/\Delta(c_p - c_v)$ is the polytropic index and $\theta = d\Delta/T_0$, and these specify the temperature gradient and depth of the polytropic layer; ρ_0 determines the total mass (per unit area) within the layer.

The expressions (2a)–(2c) provide a reference atmosphere that can be used to define convenient dimensionless units, based on d as the unit of length, the isothermal sound crossing time $[d^2/(c_p - c_v)T_0]^{1/2}$ as the unit of time, and T_0 and ρ_0 as the units of temperature and density. The dimensionless equations for the conservation of mass, momentum, and energy and the perfect gas equation can then be written as

$$\partial_t \rho + \nabla \cdot \rho u = 0 , \tag{3a}$$

$$\partial_t \rho u + \nabla \cdot \rho u u + C_k P_r T_{ao}^{1/2}(\hat{\Omega} \times \rho u) = -\nabla p$$
$$+ P_r C_k [\nabla^2 u + \tfrac{1}{3}\nabla(\nabla \cdot u)] + \theta(m + 1)\rho \hat{z} , \tag{3b}$$

$$\partial_t T + u \cdot \nabla T + (\gamma - 1)T\nabla \cdot u = \frac{\gamma C_k}{\rho} \nabla^2 T + V_\mu , \tag{3c}$$

$$p = \rho T . \tag{3d}$$

Here T, ρ, and p are the temperature, density, and pressure, $u = (u, v, w)$ is the velocity vector, $\hat{\Omega}$ and $\hat{z}$ are unit vectors, and $V_\mu = \{[(\gamma - 1)C_k]/\rho\}P_r \partial_i u_j(\partial_i u_j + \partial_j u_i - \tfrac{2}{3}\nabla \cdot u\delta_{ij})$ is the viscous heating term. The equations yield dimensionless parameters the Prandtl number $P_r = \mu c_p/K$, the ratio of specific heats $\gamma = c_p/c_v$, and the thermal dissipation parameter $C_k = K/\{d\rho_0 c_p[(c_p - c_v)T_0]^{1/2}\}$, which is the ratio of

the sound crossing time to the thermal relaxation time (assessed at $z = 0$). The Coriolis term in equation (3b) includes a parameter $[T_{ao} = 4\Omega_0^2 d^4/(\mu^2/\rho_0^2)]$, which is the standard Taylor number, $T_a = 4\Omega_0^2 d^4/\nu^2$ evaluated at the upper boundary (since $\nu = \mu/\rho$). The Taylor number defines the ratio of the viscous diffusive timescale to the imposed rotation period. For consistency with the Rayleigh number (see below), this paper quotes T_a as evaluated at midlayer in the unperturbed polytrope rather than T_{ao}.

As boundary conditions, it is asserted that the fields u, T, ρ, and p are periodic on the vertical planes positioned at $x = 0$, X_{max}, and $y = 0$, Y_{max}. Further, the upper and lower horizontal boundaries are assumed to be impermeable and stress-free, with fixed temperature on the upper one and fixed heat flux on the lower one, and thus

$$\rho w = \partial_z u = \partial_z v = 0 \text{ at } z = 0, 1 , \tag{4a}$$

$$T = 1 \text{ at } z = 0 , \quad \partial_z T = \theta \text{ at } z = 1 , \tag{4b}$$

which ensure that the mass flux and the viscous stresses vanish on the boundaries. The total mass in the computational domain is thereby conserved, and only a flux of heat is carried through the system.

The equilibrium state (2) provides a useful reference atmosphere for the model from which a number of dimensionless parameters can be calculated. Three measures of stratification and depth of the layer are the pressure scale height

$$H_p(z) = \frac{(1 + \theta z)}{\theta(m + 1)} , \tag{5}$$

whose integral is the number of pressure scale heights spanned by the layer,

$$N_p = \int_0^1 H_p^{-1}(z)dz = (m + 1)\ln(1 + \theta) , \tag{6}$$

and the ratio of the density at the lower boundary ($z = 1$) to that at the upper boundary ($z = 0$),

$$\chi_\rho = (1 + \theta)^m . \tag{7}$$

The effects of compressibility become important in the nonlinear regime when $\chi_\rho \gtrsim 10$ (e.g., Hurlburt et al. 1984).

The convective instability of the polytropic layer to disturbances is measured by the superadiabatic temperature gradient

$$(\nabla - \nabla_{ad}) = \theta\left[1 - \frac{(m+1)(\gamma-1)}{\gamma}\right]. \tag{8}$$

For a fluid of nonzero viscosity and thermal conductivity, sufficient superadiabaticity is required to overcome diffusive processes for convection to ensue; that is, the Rayleigh number,

$$R_a(z) = \frac{\theta^2(m+1)}{P_r C_k^2}\left[1 - \frac{(m+1)(\gamma-1)}{\gamma}\right](1+\theta z)^{2m-1}, \tag{9}$$

must exceed a critical value for instability (Gough et al. 1976). This critical value, R_{a_c}, increases with the stabilizing effects of rotation (Chandrasekhar 1961) as measured by the Taylor number. This paper quotes R_a evaluated at midlayer ($z = 0.5$) in the unperturbed polytrope and all R_a considered here are amply supercritical.

The energy flux through the layer in the static state is given by

$$F_T = \frac{C_k \gamma}{\gamma - 1}\theta, \tag{10}$$

which is independent of depth. It is useful to divide F_T into two contributions derived from the adiabatic and super-adiabatic parts of the temperature gradient, respectively; namely

$$F_a = F_T \frac{(\gamma-1)(m+1)}{\gamma}, \tag{11a}$$

$$F_s = F_T\left[1 - \frac{(\gamma-1)(m+1)}{\gamma}\right]. \tag{11b}$$

Because of the polytropic nature of the model considered here, F_a can be a significant fraction of the total flux.

Equations (3a)–(3c) are invariant under the transformations

$$x \to -x, \quad u \to -u, \quad \Omega_0 \to -\Omega_0, \tag{12a}$$

$$y \to -y, \quad v \to -v, \quad \phi \to -\phi, \tag{12b}$$

and their combination. This means, for example, that the results quoted here for the northern hemisphere of a star rotating in an counterclockwise motion (west to east) like our Sun apply equally well to a star rotating in the opposite direction, with the domain placed in the southern hemisphere, provided the x and y directions (and their associated velocities) are reversed (x increases westward, y increases southward). Since the compressible equations operate in a left-handed coordinate system (z points downward), positive rotation in the original calculations is clockwise when viewed from above the north pole. In presenting the results here, the more familiar rotation sense of the Sun is adopted by the transform $\Omega_0 \to -\Omega_0$, which is equivalently $u \to -u, x \to -x$.

The characteristic timescales in these problems deserve some comments. Our unit of time corresponds to the time taken by an isothermal sound wave to propagate a unit distance along the upper boundary. However, since sound speed c varies with depth, a vertically propagating sound wave has a crossing time in the unperturbed polytrope of

$$\tau_c = \int_0^1 dz\left(\frac{\rho}{p}\right)^{-1/2} = \int_0^1 dz(1+\theta z)^{-1/2} = (\sqrt{1+\theta}-1)\frac{2}{\theta}. \tag{13}$$

The thermal relaxation time for the polytropic layer is

$$\tau_k = \int_0^1 dz\left(\frac{\rho}{C_k}\right) = \int_0^1 \frac{dz(1+\theta z)^m}{C_k} = \frac{(1+\theta)^{m+1}-1}{C_k\theta(m+1)}, \tag{14}$$

whereas the timescale for viscous relaxation is given by $\tau_v = \tau_k/P_r$. Since low Prandtl number turbulent convection, in which shear instabilities and vortex stretching mechanisms are prevalent, is of most interest, the regime $\tau_c \ll \tau_k \ll \tau_v$ is explored. In the current formulation, this corresponds to small C_k and small P_r. However, with present computational resources, these simulations can reach at most a regime where these timescales differ in turn by about one order of magnitude.

The inclusion of rotation adds another timescale to the problem, namely the inertial time

$$\tau_i = \frac{2\pi}{2\Omega} = \frac{2\pi}{P_r C_k T_{a_0}^{1/2}}, \tag{15}$$

measured in units of the sound crossing time, which is the timescale for momentum oscillations induced by the Coriolis forces. Note that this is related to the rotation period, τ_r, by $\tau_i = 0.5\tau_r$.

The influence of rotation on motions is usually measured by a Rossby number, which compares the rotational time-scale to a typical fluid timescale. By interpreting the governing dimensionless parameters as ratios of timescales,

$$R_a = \frac{\tau_v \tau_k}{\tau_b^2}, \quad P_r = \frac{\tau_k}{\tau_v}, \quad T_a = 4\pi^2 \frac{\tau_v^2}{\tau_i^2}, \tag{16}$$

a "convective" Rossby number R_0 that measures the rotational influences on the ensuing convection can be formed as the ratio of the buoyancy (convective) timescale (the reduced free-fall time), τ_b, to the rotation timescale, τ_i. This yields

$$R_0 = \left(\frac{R_a}{T_a P_r}\right)^{1/2}, \tag{17}$$

which first appeared as a parameter in Gilman (1977). It is expected that R_0 less than unity implies a significant rotational influence on the convection because in the time a buoyant fluid element traverses the fluid layer it will complete more than one inertial oscillation. Convective states with rotational influence ranging from strong to weak are examined, corresponding to $0.7 \lesssim R_0 \lesssim 7$. The more familiar definition of the Rossby number, here termed the "true" Rossby number R_{0_t}, compares the root mean square (rms) vorticity ω_{rms} within the resultant convection to the planetary vorticity,

$$R_{0_t} = \omega_{rms}/2\Omega. \tag{18}$$

Note that R_0 is an external measure of the effect of rotation on the convective motion that can be determined in advance, whereas R_{0_t} can be determined only from the results of the simulation. It is found that the convective and true Rossby numbers are similar in value in these simulations.

2.2. Numerical Methods

Equations (3a)–(3d) are solved numerically as an initial value problem. The initial conditions consist of either the polytropic state (2) plus a small random perturbation of the temperature field consistent with the boundary conditions or of fields taken from a previous mature solutions nearby in parameter space.

The numerical scheme consists of a hybrid finite-difference and pseudospectral scheme in which the vertical structure is treated by fourth-order finite differences and the horizontal variations by a Fourier collocation method (see Canuto et al. 1988). Thus the requirement of periodicity in the horizontal directions is satisfied automatically by an expansion of the solution in trigonometric functions. The boundary conditions at $z = 0, 1$ are implemented in the discretized equations as finite-difference reflection conditions which are chosen to ensure that the mass flux and mechanical energy flux vanish on the boundary and that the temperature and heat flux satisfy equations (4a) and (4b). The time discretization is based on an explicit, two-level, Adams-Bashforth scheme (see Richtmyer & Morton 1967). An exception is the thermal conduction term on the right-hand side of equation (3c), which is treated by an implicit Crank-Nicholson scheme in order to avoid an overly restrictive time step constraint resulting from the low density at the upper boundary. The time stepping and the evaluation of derivatives occurs in (k_x, k_y, z) space (where k_x and k_y are the horizontal wavenumbers). Products of the field variables and their derivatives are calculated in configuration (x, y, z) space, with the transformations between the two spaces afforded by fast Fourier transform techniques.

3. RESULTS

A series of runs has been made sparsely populating the four-dimensional parameter space (R_a, T_a, P_r, ϕ) of the local model, but revealing a rich set of results. The parameters for these runs are summarized in Table 1. All simulations were computed with an aspect ratio of 4:4:1, with $\gamma = 5/3$, and with an initial density contrast of $\chi_\rho = 11$ so that the layer spans roughly 5 pressure scale heights (although the layer relaxes from initial conditions to a typical value of $\chi_\rho \sim 20$). These initial conditions correspond to a polytrope with $\theta = 10$ and $m = 1$. The Rayleigh number is then changed by altering C_k and keeping P_r small

such that $\tau_c < \tau_\kappa < \tau_\nu$ at fixed θ, effectively changing the fluid for a given forcing. The degree of instability, as measured by the departure of the Rayleigh number from the linear critical value, $R_a - R_{a_c}$, is not necessarily kept fixed when varying other parameters. For instance, studying the influence of the rotation by changing the Taylor number and keeping all other parameters fixed alters the convective Rossby number as desired. However, the degree of nonlinearity is also affected, since the linear critical value for the onset of convection is a function of Taylor number. Similarly, changing the latitude while keeping the other parameters fixed also affects $R_a - R_{a_c}$. However, since highly nonlinear regimes are studied here, the relative differences in supercriticality are minor. Values of $(R_a - R_{a_c})/R_{a_c}$ are shown in Table 1, where R_{a_c} is calculated for the most unstable mode (direct or oscillatory) by inverse iteration over parameter space.

In addition to the external control parameters, the degree of turbulence encountered in the resulting solutions must be determined. The standard dimensionless parameter for this is a Reynolds number, which indicates the relative balance between advective and diffusive processes. This may be defined by

$$R_e(z) = \frac{U(z)\bar{\rho}(z)l}{C_k P_r},\qquad(19)$$

where l and $U(z)$ are a typical length and velocity, respectively. In the current context, a problem arises as to how to choose these typical values. If the length scale is chosen as the depth of the domain, a typical velocity may be evaluated as the (time-averaged) rms velocity, U_{rms}, or as the maximum velocity attained in the box, U_{max}, in order to create a Reynolds number. Table 1 shows values of $R_{e_{rms}}$ and $R_{e_{max}}$ corresponding to the above definitions respectively for each case. It is useful also to quote in Table 1 a Reynolds number, R_{e_λ}, based on the Taylor microscale, λ combined with U_{rms}. The latter length scale, defined as

$$\lambda^{-2}(z) = \overline{V_\mu}(z)/U_{rms}(z),\qquad(20)$$

represents the scale of dissipation associated with the rms velocity rather than the scale of the domain. These measures still indirectly include an indication of the stabilizing effect of rotation: increased rotational influence (for fixed R_a) decreases the scales of the fluid motion and therefore decreases any Reynolds number. In general here, a value of

TABLE 1

PARAMETERS FOR THE f-PLANE ROTATING CONVECTION SIMULATIONS

Case	R_a	T_a	P_r	ϕ	(n_x, n_y, n_z)	R_0	$\dfrac{(R_a - R_{a_c})}{R_{a_c}}$	R_{e_λ}	$R_{e_{rms}}$	$R_{e_{max}}$
L1	5×10^4	3×10^4	$10^{-1/2}$	45	$64 \times 64 \times 32$	2.29	9.23	3.06	141	372
L2	5×10^4	3×10^4	$10^{-1/2}$	90	$64 \times 64 \times 32$	2.29	2.78	2.40	120	318
L3	5×10^4	3×10^4	$10^{-1/2}$	15	$64 \times 64 \times 32$	2.29	21.5	4.36	169	377
R0	5×10^5	0	0.1	0	$192 \times 192 \times 130$	∞	420	14.03	932	2877
R1	5×10^5	10^5	0.1	45	$96 \times 96 \times 64$	7.07	182	12.85	932	2972
R2	5×10^5	10^6	0.1	45	$96 \times 96 \times 64$	2.24	111	8.72	764	2451
R3	10^7	5×10^7	0.1	45	$256 \times 256 \times 129$	1.41	109	11.33	2068	7621
R4	5×10^5	10^7	0.1	45	$96 \times 96 \times 64$	0.71	29.2	7.49	609	2068
R5	5×10^5	10^7	0.1	15	$96 \times 96 \times 64$	0.71	52.9	4.01	784	2383
R6	5×10^5	10^7	0.1	75	$96 \times 96 \times 64$	0.71	18.0	3.30	675	2053
T1	5×10^6	10^7	0.1	45	$192 \times 192 \times 96$	2.24	292	11.45	1703	5828
T2	10^7	2×10^7	0.1	45	$256 \times 256 \times 130$	2.24	378	11.83	2149	8108

R_{e_λ} greater than about 10, or $R_{e_{rms}}$ and $R_{e_{max}}$ of about 10^3 or greater indicates a solution which is at least moderately turbulent.

The solutions described in Table 1 are divided into three categories, annotated with a prefix of either L, R, or T. Cases labeled L are laminar by any measurement, whereas all other cases are turbulent in some sense but to varying degrees, with cases labeled T being the most obviously turbulent cases. Cases R0–R4 are a series of solutions where the rotational influence (as measured by R_0) is increasing for a fixed latitude, whereas cases R4–R6 maintain a strong rotational influence while varying the latitudinal positioning of the local model on the sphere.

3.1. Overview of Structure of Turbulent Convection

This current work was prompted in part by that of Cattaneo et al. (1991), which examined the differences between laminar and turbulent compressible convection achieved in the absence of rotation. In that study, turbulent calculations exhibit a cellular convective network at the surface which persist from the laminar solutions. The network consists of broad, warm upflowing regions delineated by narrow, cold downflowing lanes joined in an irregular polygonal pattern. This connected network remains quasi-steady, with shallower downflowing features being advected into the lanes by the diverging upflows. The cellular upper surface in a turbulent case serves to disguise an interior consisting of small-scale, turbulent, horizontally isotropic motions. The appearance of these turbulent motions is not due to the dependence of the diffusivities on the density stratification. Code 1 of Cattaneo et al. 1991 uses a constant dynamic viscosity (diffusivity $\sim 1/\rho$), whereas code 2 operates with (an effective) constant kinematic viscosity (diffusivity constant). Both codes produce qualitatively similar results, with the small-scale fluctuations more likely being produced by shear instabilities of the rapid downflows. The laminar surface layer is a consequence of the rapidly decreasing density with height, with the rapid expansion of fluid elements nearing the surface smoothing out the small-scale fluctuations. The convection also generates plume-like structures which span the full vertical extent of the layer. These structures are coherent in both space and time and are associated with the interstices of the quasi-steady downflow network at the surface. A major result of that paper is that the total convective energy transport for the turbulent cases is achieved dominantly by the small-scale turbulent motions in the interior rather than by these coherent structures.

With the inclusion of the effects of rotation, turbulent compressible convection maintains a similar overall configuration (but with some significant modifications, discussed in the following sections). Figure 2 presents an instantaneous perspective view of the vertical velocity in the full computational domain for a typical calculation (T2). Downflow is shown as dark tones and upflow as light. The granular, laminar upper layers are evident at the top surface, and the side panels reveal that (dark) features stemming from the downflowing lanes can penetrate the full depth of the layer. Also apparent is the change of scale with depth. The surface cells give way to smaller scales in the interior, as shown clearly in the plane displaced from the neighborhood of the lower boundary.

Figure 3 reveals these varying scales with depth in greater detail. This figure presents the vertical velocity, tem-
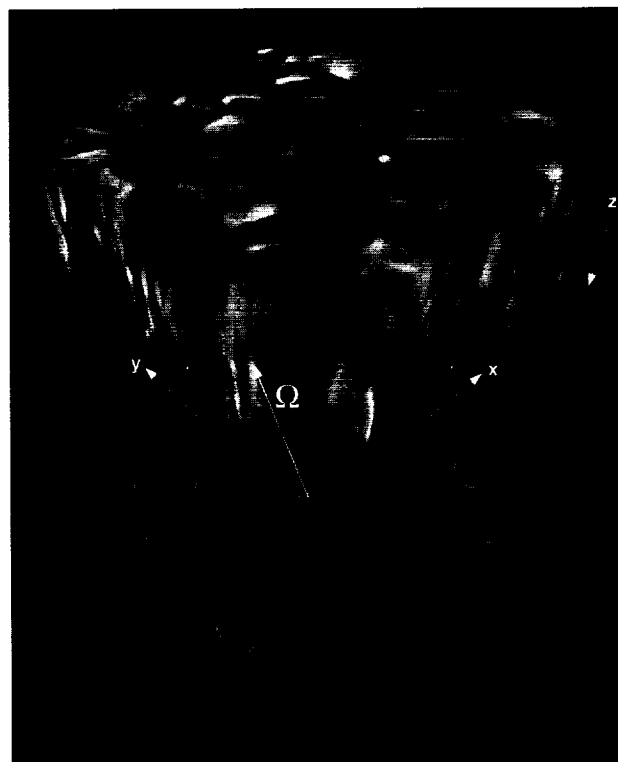

FIG. 2.—Perspective view of a typical solution of three-dimensional turbulent compressible convection with rotation on an f-plane, showing the vertical velocity w on the faces of the computational domain at one instant in time within simulation T2. Dark tones indicate downflows and lighter tones upflows. A horizontal plane near the lower boundary is displaced to show the smaller scale turbulence at depth. The flows near the upper boundary have a smooth laminar appearance, with curving networks of downflow involving cyclonic vortices of fast downflow at their interstices. The side panels reveal that the more prominent downflow plumes from the surface extend to the bottom of the layer.

perature, density, and vertical vorticity fields on three horizontal slices through the domain taken near the top, at the middle, and close to the bottom of the layer. The slices are individually gray-scaled so that positive values are displayed as light tones and negative are dark (with the vertical velocity reversed for clarity since by convention w is positive downward). The transition from a laminar surface to a turbulent interior is clearly evident, especially in the vertical vorticity fields. Near the upper surface, the vorticity is concentrated into the downflow lanes, with particular concentration at the interstices. As the network lanes break up with depth, the vorticity becomes more wide spread, until deeper down it becomes randomly distributed across the entire domain. The thermodynamic fields of temperature and density as viewed as fluctuations about their horizontal means retain a stronger imprint of the upper surface features and exhibit the turbulence as high-frequency variations superimposed on those larger scales. The distinction between the velocity and thermodynamic scales can be explained in terms of the Prandtl number. Since $P_r = 0.1$ for all these calculations, the thermal diffusivity is 10 times greater than the viscous diffusivity, thus smoothing out the thermodynamic fluctuations faster.

The division of the domain into a laminar cellular surface network superimposed upon a turbulent interior punctuated by vertically coherent structures is thus retained with the inclusion of rotation effects. However, the temporal and
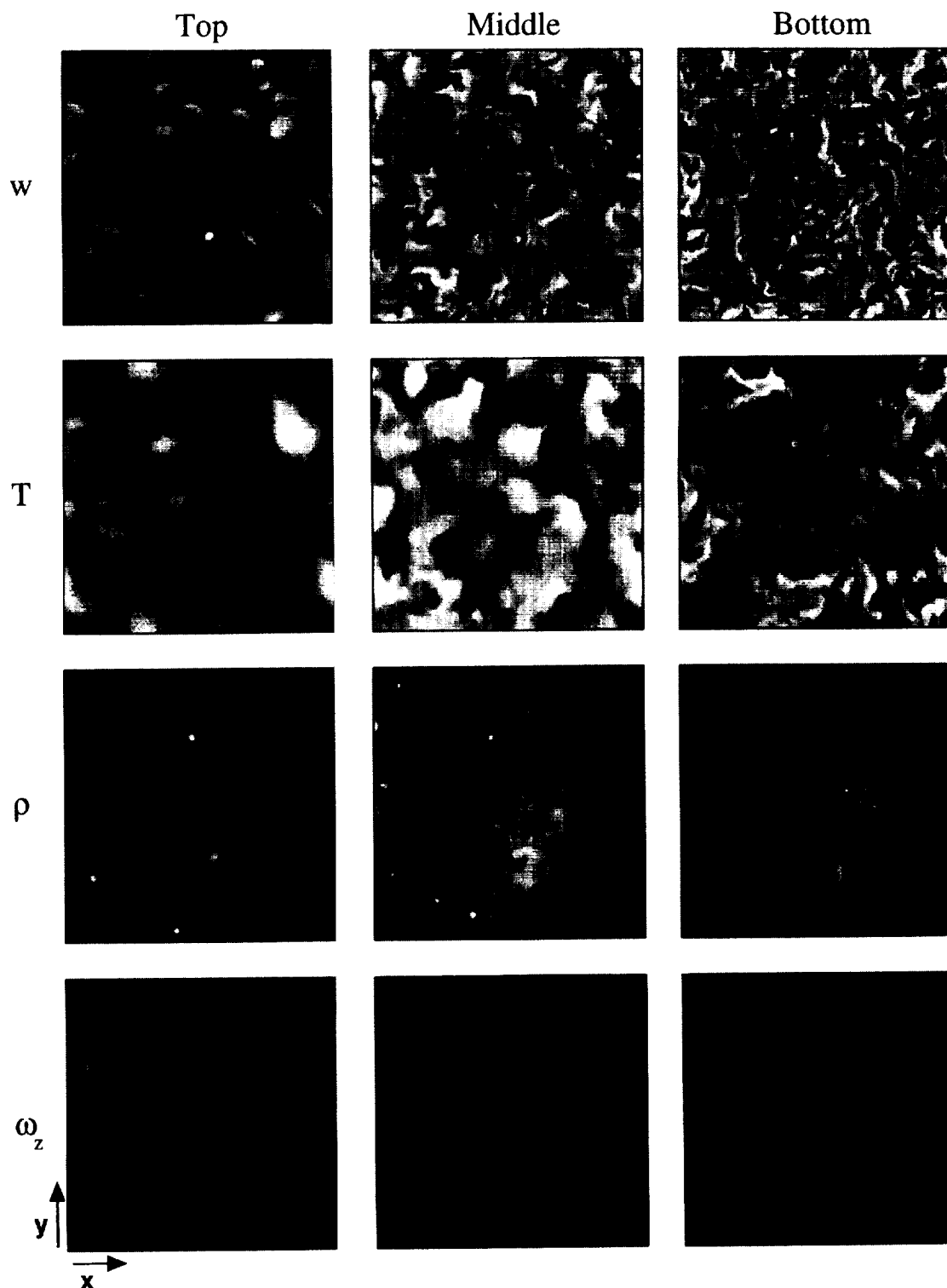
FIG. 3.—Companion to Fig. 2, showing horizontal $(x - y)$ planar views of the vertical velocity w, temperature fluctuations T', density fluctuations ρ', and vertical vorticity ω_z near the top, middle, and bottom (positioned at depths $z = 0.1, 0.5, 0.9$) at the same instant within simulation T2. Darker tones represent in turn downflowing, relatively cool, relatively dense fluid, and positive (cyclonic) vorticity, and lighter tones the opposite. The laminar appearance of the convection near the surface, involving curved cool downflow lanes and broad regions of warm upflow, is replaced by finer scale turbulent structure at greater depths. Prominent cyclonic vortices with warm, partially evacuated cores occur at many of the network junctions and form coherent downflow structures which extend over the multiple scale heights of the layer.

spatial characteristics of both the surface and the interior flows are significantly but subtly altered.

3.2. Evolution of Surface Networks and Dynamical Buoyancy

The instantaneous snapshots of the near-surface fields in Figure 3 already reveal apparent differences. In the vertical velocity, the network of downflowing lanes are now more curvaceous than the straight, polygonal boundaries of the nonrotating cases. The intersections of the downflow network are also much less distinct, with lanes ending in cusps or apparently floating without connection. The reason for the existence of such features becomes more

obvious in a time sequence of the surface pattern. Figure 4 shows the evolution of the near-surface vertical velocity at 12 equally spaced time intervals spanning 7.83 sound crossing times, corresponding to roughly 2 large-scale turnover times. In such rotating compressible convection, the gradual evolution of the surface network observed in non-

rotating cases is no longer realized. Here no distinct cellular pattern can be identified for much longer than a convective turnover time. The inclusion of the background (or "planetary," in the geophysical context) vorticity from the rotating frame leads to swirling motions of various sections of the network, thereby displacing and destroying the
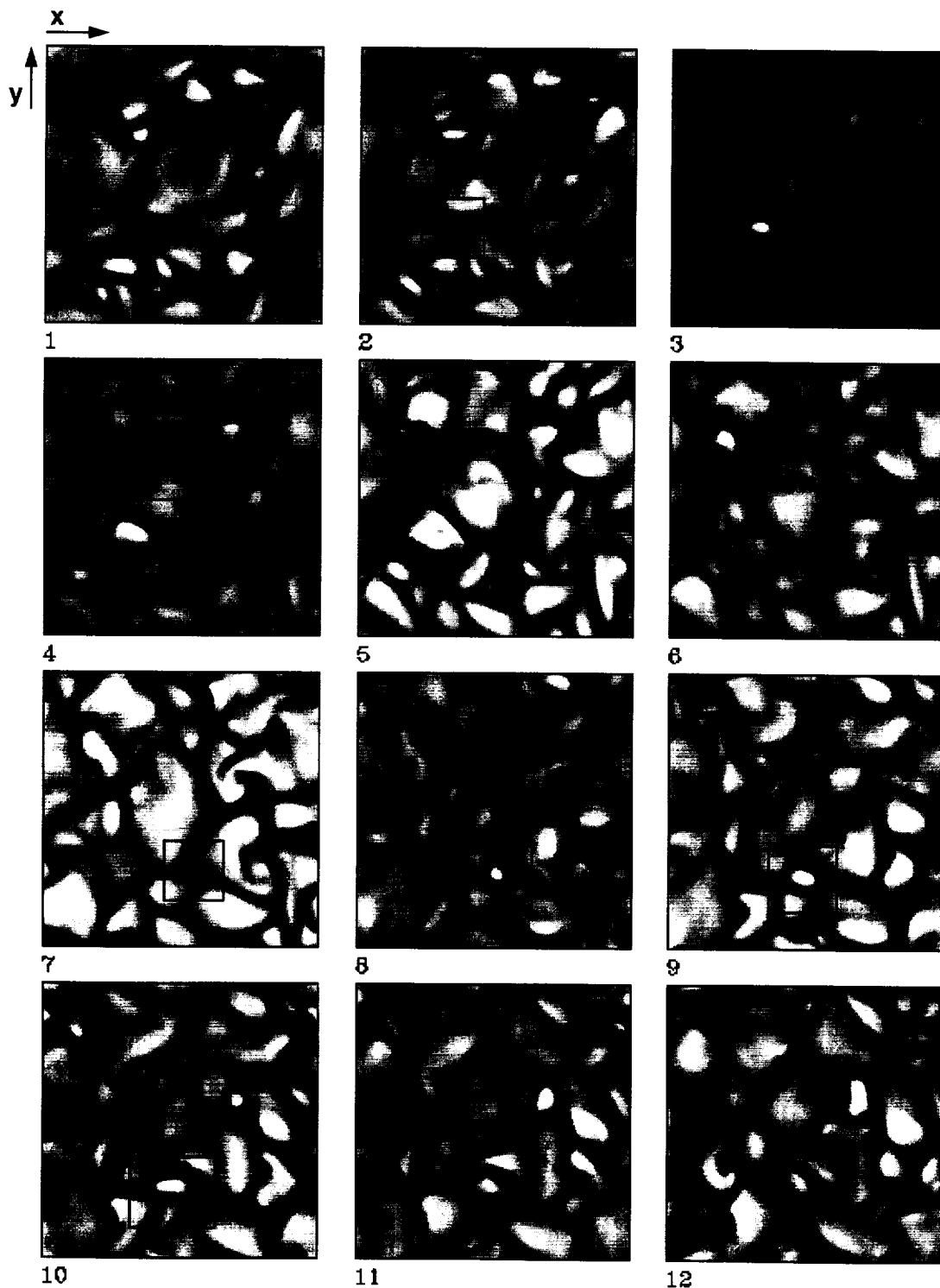
FIG. 4.—Time sequence of the vertical velocity in horizontal planar views near the top surface within the turbulent simulation T1. The equally spaced 12 time samples span 7.83 time units. Two sites are outlined that illustrate the evolution of strong cyclonic vortices of downflow (darker tones). Dynamical buoyancy leads to flow reversal at their cores (upflow in lighter tones) and subsequent disintegration, with some replaced by expanding upflows that form new cells. Detailed comparison of succeeding images shows that the patterns evolve quite rapidly, partially aided by the churning motions associated with inertial oscillations (of period ~ 5.44 time units here at the surface) induced by Coriolis forces.

temporal coherence. These churning motions are due to inertial oscillations of larger scale flows, in particular the mean horizontal shearing flows that are generated by the action of rotation on the convection (discussed in detail in Paper II). The inertial displacements of various sections of the pattern are not necessarily in phase and so the overall pattern is distorted, broken, and reformed on the inertial timescale, destroying any long-term temporal coherence.

A feature of the near-surface flows that is noticeably enhanced by the presence of the background rotation is the ability of the intersections of the downflowing lanes to self-destruct by the dynamical buoyancy (Parker 1991; Arendt 1993) action of the vertical vorticity. The near-surface snapshots of Figure 3 demonstrate that the junctions of downflowing cellular lanes may exhibit a curly, eye-like or hooked appearance in w and T. Related behavior is also noted in the magnetoconvection simulations of Brandenburg et al. (1995). Such occurrences here coincide with distinctive patches of low density (bright points in the density image) and strong cyclonic (dark) vertical vorticity. The time series of vertical velocity images in Figure 4 shows that such structures are events during the destruction of a network junction. The small outlined boxes within the time-sequence images of Figure 4 coarsely pick out the life history of two specific examples. This evolution is presented in more detail in Figure 5, which provides a composite picture of a typical destruction event. A time sequence is shown (with time increasing down the page) of the vertical velocity, the verti-

cal vorticity and the relative thermodynamic fluctuations (scaled by their horizontal mean values at that depth), along with the rate of buoyancy work W_b (the product of vertical velocity and density fluctuations, $w\rho'$), for a small subsection of simulation R3 near the surface. All variables are scaled such that zero lies in the middle of the gray scale, with dark tones representing negative values and bright tones positive (here w remains positive downward). Initially there exists a junction of two or three downflow lanes carrying cold and dense material downward, resulting in a positive buoyancy work there. The lanes contain substantial positive vertical vorticity which has been spun up by compression under the action of Coriolis forces and is concentrated at the interstices of the network. If the vortices that are created at the interstices spin fast enough, as is frequently the case when aided by background rotation, they evacuate the interior of the vortex leaving a low density, low pressure region. The vertical density contrast between the core and the deeper ambient fluid thus created can then start a reversal of the flow, siphoning up fluid from below and turning the vortex core into an upflow.

Parker (1991) refers to the driving of motions by the evacuation of vortex cores as dynamical buoyancy, although his work concentrated on the vertical rise of a horizontally orientated vortex that evacuates in a compressible fluid. The mechanism is similar here although the dynamics are different since the density effects occur within vertically orientated vortex tubes. In the current scenario, the whole vertical vortex is still relatively cold compared to its sur-
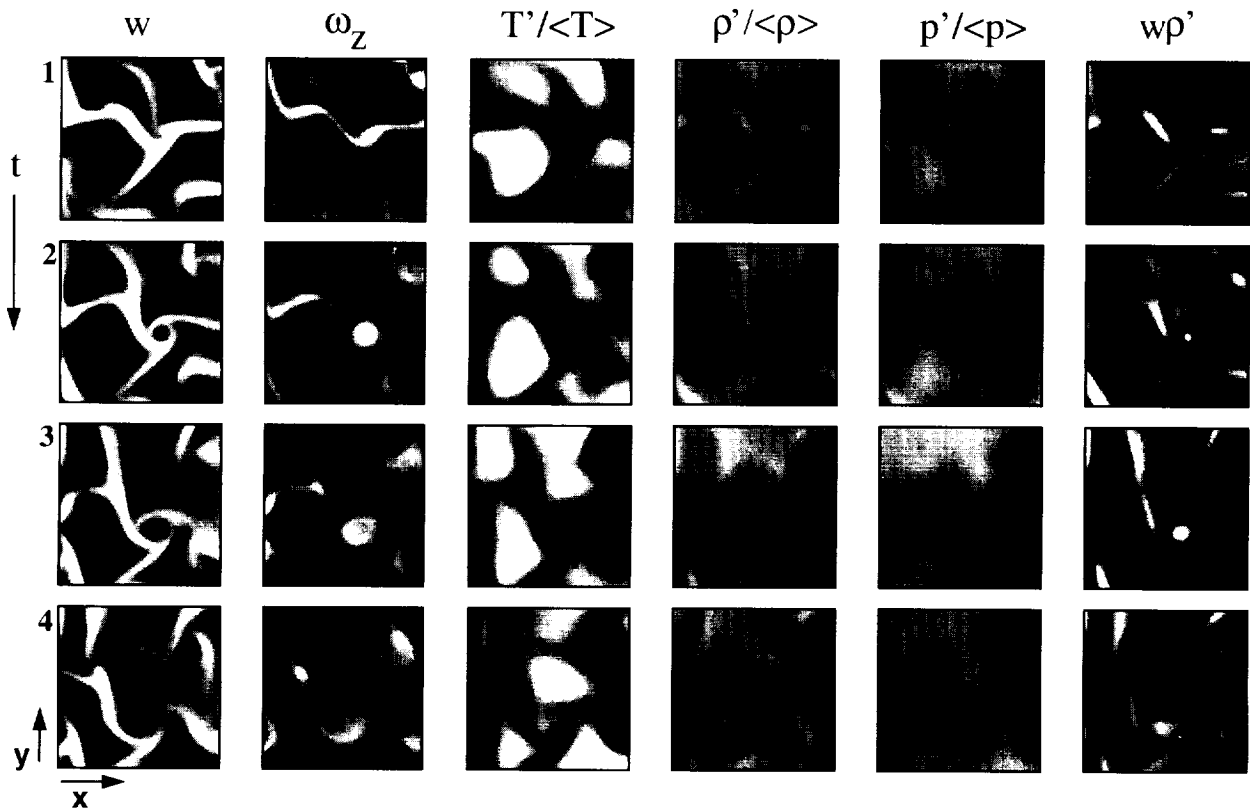

Fig. 5.—Four successive time samplings of six variables in a close-up horizontal planar view of the surface network in simulation R3, demonstrating a typical life cycle in the formation and destruction of a strong dynamically buoyant vortex at the junction of three downflow lanes. Time advances down the figure, with the samples spanning 2.35 time units [compared to $\tau_i(z = 0) \sim 3.44$]. The variables shown are the vertical velocity, the vertical vorticity, and relative temperature, density, and pressure fluctuations (scaled by their horizontal mean values), and the rate of buoyancy work. The gray scale is such that positive values are light and negative values are dark, with w retaining its defined directionality (downflow is light, in contrast to previous plots).

roundings since it resulted from a downflow, but the central core is warmed by fluid rising from below through the tube. The flow in the surrounding vortex sheath is still downward and is now marked by a region of negative buoyancy work since this downflowing tube carries the relatively low density gas. The core exerts positive buoyancy work as the less dense gas is carried upward, although it is quickly flung outward by the rapid local rotation of the strong vertical vorticity. The action of the upflowing core tends to destabilize the vortex since the surrounding sheath is pushed apart by the expansion of the upflowing core (and its ultimate divergence at the surface). This mechanism offers one route by which the interstices are destroyed and new cells (as defined by a broad upflow) are created. The destabilization of the junction vortices occurs through a compressible mechanism (dynamical buoyancy), suggesting that incompressible calculations may yield more stable examples of strongly spinning plumes. This mechanism is commonly witnessed in these simulations even when the rotational influence is weak. Even without rotation, strong vorticity at lane junctions forms weakly evacuated vortices and some flow reversal but tends not to break up the structure. Greater local velocities would be required to initiate such effects when there is no background pool of vorticity to draw upon.

The temporal dynamics of the laminarized surface cellular network are thus distinctly different in the presence of rotation. There is a loss of temporal coherence of the network, a different cellular topology, and enhanced cell creation (and network destruction) mechanisms.

3.3. Vorticity Structure at Greater Depths

Turbulence within incompressible simulations has been shown to involve intense vortex structures or "tubes" (e.g., She, Jackson, & Orszag 1990; Vincent & Meneguzzi 1991). Compressible studies of homogeneous and convective turbulence with the nearly inviscid Piecewise Parabolic Method (PPM) (e.g., Pouquet, Porter, & Woodward 1994; Porter & Woodward 1996) also exhibit vortex tube formation. The convective turbulence in this study is no exception to this now common structural characterization. Figure 6 (see Plate 16) shows volume rendering of snapshots of enstrophy (magnitude of vorticity squared) for nonrotating (R0) and rotating (T2) turbulent simulations at comparable degrees of supercriticality. Here color and opacity values have been ascribed to each point according to the amplitude of the enstrophy. Brighter, more opaque patches are associated with strong vortex structures whereas dark, translucent regions are areas of weak or vanishing enstrophy.

Differences between nonrotating and rotating turbulent convection may be noted in their vortex characteristics exhibited in Figure 6. With no rotation, the domain is populated sparsely by a few very straight and coherent large vertical vortex tubes or "chimneys." These are associated with the strong, vertically, and temporally coherent downflows which are generated at the interstices of the surface network. These tubes penetrate a turbulent interior that is composed of many small-scale vortices. The latter are especially prevalent around the strong downflowing structures, which suggests a generation of vorticity by instabilities of those coherent structures. However, for this nonrotating case, the small-scale vortex tubes are not very distinct and are preferentially vertically aligned, with few horizontally orientated structures in existence. The rotating case reveals a much busier and more random structuring in the enstrophy field. This is rather remarkable since the nonrotating solution actually has a higher degree of supercriticality and a higher measured R_{e_λ}. With rotation, the enstrophy field again involves vertically coherent, large vortices penetrating much of the domain, co-existing with small-scale vortex tubes in the deeper interior. The number of large, coherent tubes has increased, reflecting a reduction of the preferred wavelength with the increase in Taylor number (cf. Chandrasekhar 1961). Likewise, the width of such structures has also decreased. Most noticeably, the tubes in the interior have become more intense and thus more distinct in structure.

Figure 7 (see Plate 17) shows details of the enstrophy structure extracted from a full domain of the rotating simulation T1. The increase in the number of large-scale coherent vortices and their inertial motions engendered by the rotation leads to strong interactions between the structures, which are evident in the close-up view in Figure 7a, which focuses in on a unit cube subsection in which a number of strong chimneys are interacting. These intense quasi-two-dimensional vortices are mutually advected by each others flow fields and by the inertial flows. The vortices may then interact in a manner resembling two-dimensional vortex dynamics. Since the vortices are all associated with strong downflow sites and therefore with velocity convergence (enhanced by the stratification as the fluid descends), they must all spin cyclonically (i.e., in the same sense as the rotation) due to the action of Coriolis forces. Like-signed vortices can merge whereas oppositely signed vortices repel each other, and thus the coherent structures present here will preferentially combine. Coherent downflow sites become a tangle of interwoven strong vortex tubes with subsequent increase in complexity of small-scale vorticity generation in the interior. Turbulent f-plane rotating Boussinesq convection with a vertical rotation vector exhibits similar vortex dynamics (Julien et al. 1996) in the absence of compressible effects. Figure 7b shows a view from above of the enstrophy field, encompassing the full horizontal extent but only the upper quarter of the domain in the vertical. The strong vortex chimneys at the interstices of the upper network are connected by twin vortex sheets or horizontally orientated vortex tube pairs. These vortex sheets or tubes (of opposite sense) are formed at the edges of the downflow lanes within the upper thermal boundary layer. The tubes exhibit vortex stretching instabilities, the presence of which is accentuated when the Prandtl number P_r is very small, as in PPM simulations (Porter & Woodward 1996). The vortex stretching leads to complex structures that are advected by the larger scale flows, which, along with the entwining of tubes in the interactions between imperfectly balanced large-scale tubes, leaves tubes at various orientations at greater depths shown in Figure 7c.

Comparison of Figures 7b and 7c emphasizes that the appearance of the enstrophy field changes dramatically with depth. The small-scale vortex tubes ubiquitous in turbulence dominate the scene in the lower portion of the layer. The tubes are twisted, curved, and scattered with very little apparent preferential alignment, evidently existing with both horizontal and vertical orientation with equal likelihood. Contrast this with the strong vertical bias of the nonrotating case. The Coriolis terms in the momentum equation provide a linear mechanism for transferring momentum (and consequently vorticity) between the verti-
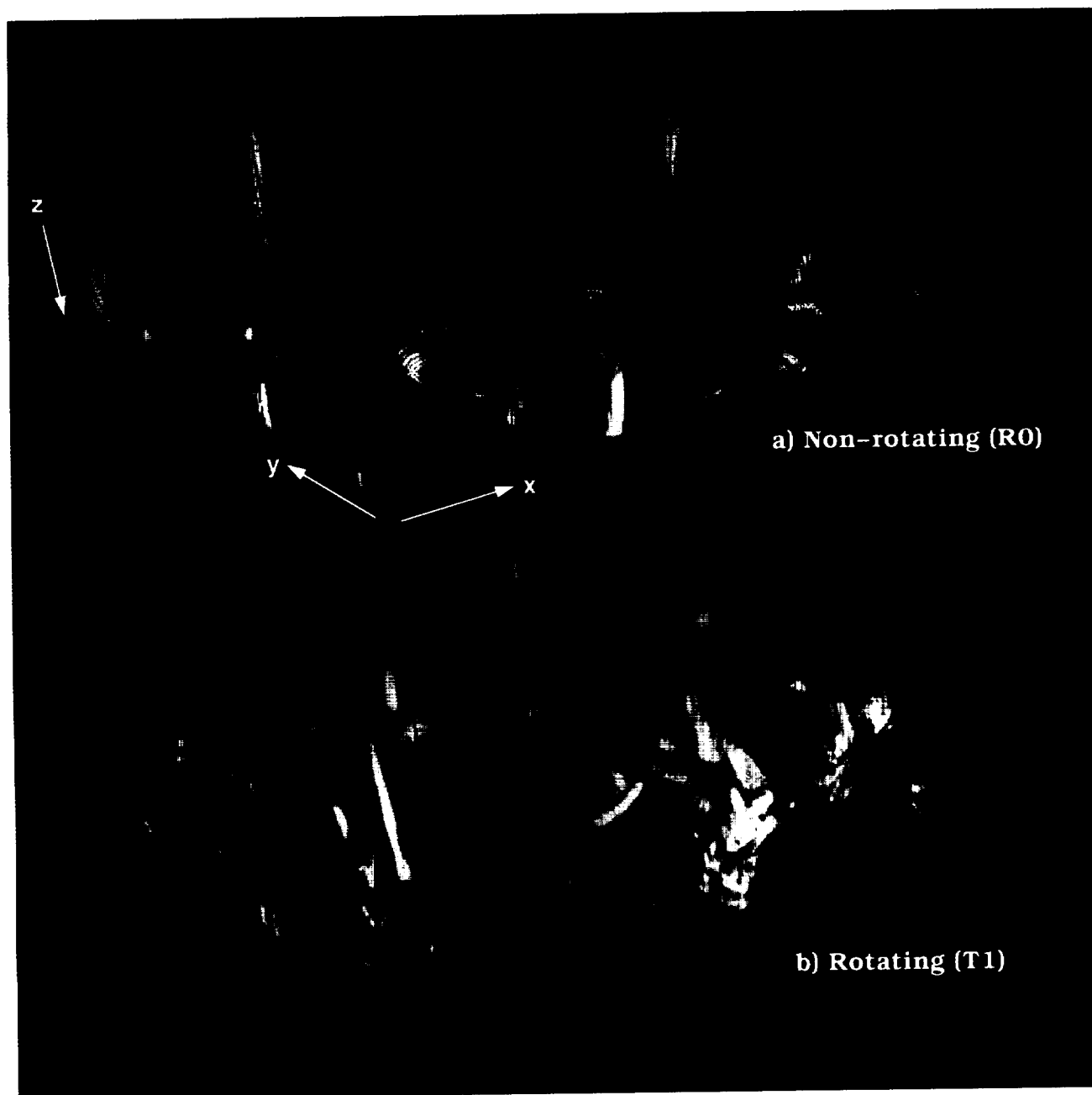
PLATE 16

FIG. 6.—Volume rendering of enstrophy (vorticity squared) at a typical time in comparable (a) nonrotating (case R0) and (b) rotating (case T2) turbulent simulations, showing 4:4:1 computational domains. Bright and opaque colors represent strong enstrophy; dark and translucent tones represent weak enstrophy. In the absence of rotation, the convection involves widely spaced and primarily upright coherent vortex tubes or "chimneys" of downflow, surrounded by smaller scale enstrophy structures. With rotation, the spacing is considerably reduced between the strong cyclonic chimneys, which have a tendency to align with the rotation vector for sufficiently strong rotation. The interior is laced with distinct intense small-scale vortex tubes with more random orientation.

BRUMMELL, HURLBERT, & TOOMRE (see 473, 504)

PLATE 17
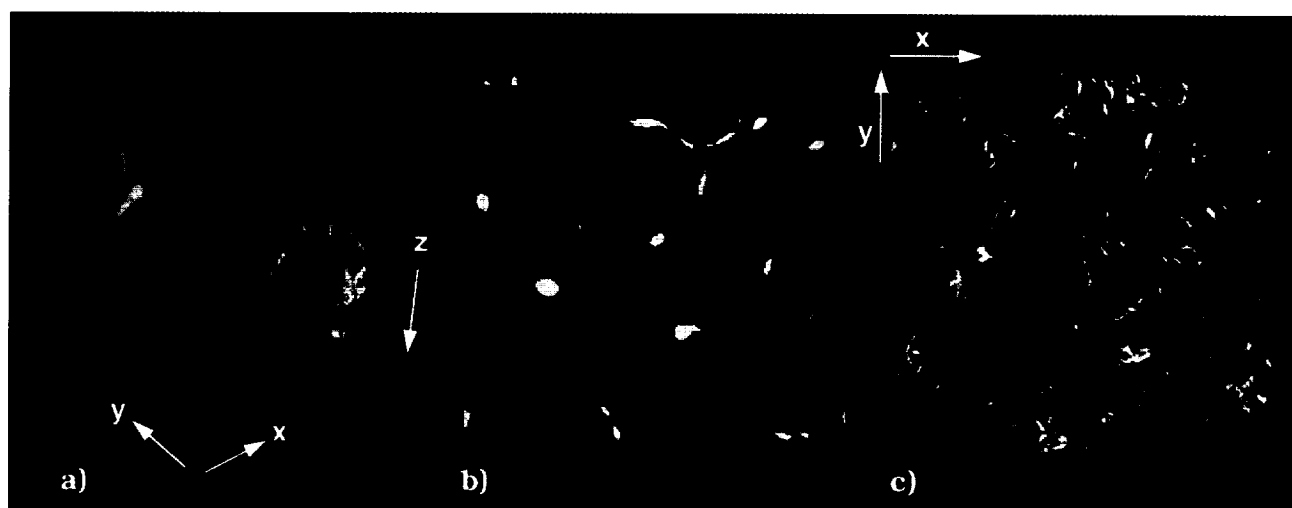
FIG. 7.—As in Fig. 6, volume rendering of enstrophy at a typical time in the turbulent rotating simulation T1. Panel (a) shows details of enstrophy structuring within a unit cube extracted from the full domain, revealing interactions between strong vortex chimneys that merge or yield intertwined structures. The adjoining panels show enstrophy in shallow horizontal segments of full width viewed from above for (b) the upper quarter of the domain and (c) the bottom quarter. Near the top of the layer, double vortex sheets or horizontally orientated tube pairs are associated with the downflow networks surrounding the broad ascending regions of warm upflow, with prominent cyclonic vorticity again positioned at the interstices of the network. Deeper in the layer the structure of the vorticity field is more complex, involving both coherent chimneys of vortical downflow interspersed with smaller scale intense vortex tubes at various orientations.

BRUMMELL, HURLBERT, & TOOMRE (see 473, 504)

cal and horizontal components and thus enhance mixing. In the absence of rotation, only nonlinear mechanisms can achieve this transfer. Some degree of large-scale intermittency is exhibited in this enstrophy field associated with the generation of these tubes from the more discrete sites at the upper boundary. Note that the chimneys at the upper surface and smaller scale vortex tubes near the lower surface are preferentially vertically aligned by the nature of the boundary conditions. Stress-free bounding surfaces allow only vorticity perpendicular to that surface, and hence tubes must emanate vertically from the horizontal boundaries. A rigid boundary condition ($u = 0$ at $z = 0$, 1) suffers similarly by disallowing vertical vorticity in favor of horizontal vorticity. Only a "soft" or penetrative boundary condition, where the layer is surrounded by otherwise stable fluid, would allow vortex tubes of all orientations at the interface.

An unanswered question is whether the small-scale, intense turbulence in the interior is created as an instability of the large-scale flow, or whether it is driven directly by thermal instability at the lower boundary. If the latter mechanism were responsible, then the turbulence would result from plumes breaking off from the lower boundary layer. With rotation, since these are converging flows, such plumes are spun up cyclonically. However, as these plumes leave the boundary layer and travel vertically they should expand by virtue of the stratification (although not dramatically since the scale height is large deep in the domain). An anticyclonic retardation would be applied to the cyclonic plumes by Coriolis forces acting on the expanding structures. The competition of these two mechanisms suggests that if the interior turbulence were to be created by plume formation at the lower boundary, then it would be suppressed somewhat in the rotational cases. Judging from the current simulations, the opposite appears to be true. The interior turbulence appears more intense in the rotating case, possibly due to the rotational spin-up of converging fluid elements in the background vorticity. This, along with the spatial intermittency of the turbulence, then seems to imply that instabilities of the strong, coherent downflowing regions are the more likely culprits for generation of this internal turbulence, with the large-scale flow itself being driven thermally. Indeed, two-dimensional compressible

simulations of localized buoyantly driven plumes (Rast 1996) show that such structures go shear unstable very quickly even in a quiescent background.

3.4. Mixing in the Interior

The vortex interactions enhanced by effects of rotation create interesting consequences for the mixing properties of the convection. This can be seen in Figure 8a, which presents the mean entropy profiles with depth for simulations with varying rotational influence R_0 at fixed but highly supercritical R_a. All the convection solutions involve entropy (and thermal) boundary layers at the top and bottom of the layer, with the upper ones much broader due to the greater thermal diffusivity ($\sim 1/\rho$) there. Without the effects of rotation, the two boundary layers are joined by an isentropic interior since efficient convection serves to yield an adiabatic mean stratification, as seen for the R0 case in Figure 8a (and in Fig. 1 of Cattaneo et al. 1991). Surprisingly, as the rotational influence is intensified (cases R1–R4), the entropy profile in the interior increasingly departs from an adiabatic stratification. This effect was previously noticed by Julien et al. (1996) for the equivalent rotating Boussinesq dynamics. It appears that the horizontal mixing of thermodynamic properties is enhanced by the interaction of the coherent plume-like structures, leading to a decrease in correlation between temperature fluctuations and vertical velocities. The enthalpy transport, $F_e = [\gamma/(\gamma - 1)]\overline{\rho w T'}$ (where T' is the fluctuation of temperature away from its mean $\bar{T}$; an overbar denotes a horizontal average), is therefore reduced, retarding the vertical homogenization of entropy and requiring the mean thermal field $\bar{T}$ to carry a greater radiative flux, $F_r = c_k[\gamma/(\gamma - 1)]\partial_z \bar{T}$, by becoming superadiabatic in its gradient. Figure 8b demonstrates this increasing role of the radiative flux F_r with respect to the enthalpy flux F_e number by exhibiting the decreasing ratio of these two quantities with decreasing Rossby number. Here the increasing T_a for fixed R_a and P_r implies a decrease in supercriticality, but all solutions are sufficiently nonlinear that the interior would be well mixed (isentropic) but for the effects of rotation. The resultant entropy gradients seen in Figure 8a for decreasing R_0 are intriguing since they imply that the convective flows in the
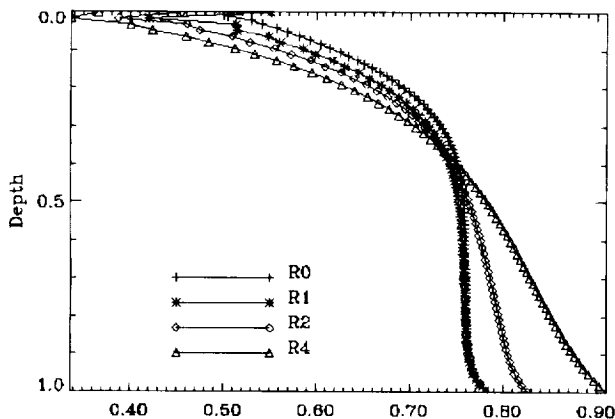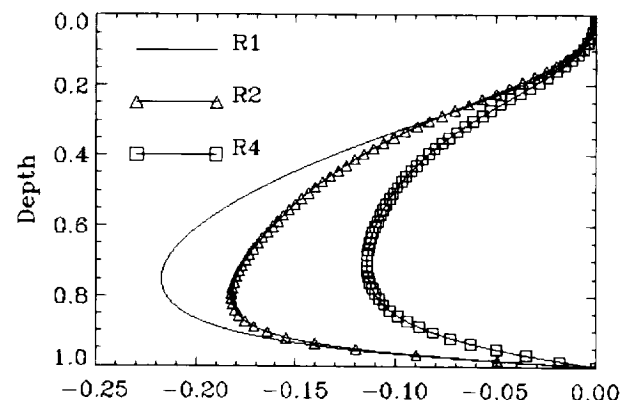
Fig. 8a

Fig. 8b

Fig. 8.—(a) Mean entropy profiles with depth, obtained by horizontal and time averaging, within the four simulations R0, R1, R2, and R4 of increasing rotational influence. All possess entropy boundary layers near the top and bottom, with the former more prominent since the thermal diffusivity is greater there. The interior is nearly adiabatically stratified when rotation effects are weak but becomes superadiabatic with decreasing Rossby number R_0 due to lateral mixing achieved by vortex interactions. (b) Associated profiles of the ratio of the mean enthalpy flux F_e to radiative flux F_r within three of those simulations.

interior can be buoyantly driven rather than adiabatically neutral.

A further interesting issue arises. Does rotation introduce a degree of anisotropy to the motions (i.e., a preferred direction), or is mixing of momentum toward isotropy enhanced? Curiously, both occur, with rotation enforcing an orientation on the large scales and yet tending to homogenize the smaller scales. To address the latter, two quantities discussed in Cattaneo et al. (1991) are useful, namely,

$$r_e(z) = \overline{w^2}/(\overline{u^2} + \overline{v^2}) , \qquad (21a)$$

$$r_\omega(z) = (\overline{\omega_x^2} + \overline{\omega_y^2})/\overline{\omega_z} . \qquad (21b)$$

The measure r_e describes the ratio of the kinetic energy (neglecting density variations) in the vertical motions to that in the horizontal motions. Similarly, r_ω is the ratio of the enstrophy associated with the horizontal vorticity to that associated with the vertical component. If the flow were completely isotropic, then r_e and r_ω would assume equipartition values of 0.5 and 2.0, respectively. Figure 9 shows the dependence of r_e and r_ω with depth (averaged over time) for four different simulations (R0–R4) with varying R_0. Increasing the influence of the rotation reduces the peak kinetic energy ratio r_e in the interior and boosts r_e near the boundaries (in general) toward that of equipartition (dotted lines in Fig. 9). The rotationally influenced flows also possess enstrophy ratios r_ω which are distributed more closely around the equipartition value.

These measures confirm the visual impression of a more random orientation of the small-scale enstrophy structures in Figure 6b. In rotating convection where a tilted rotation vector exists, the horizontal component of rotation provides a linear mechanism which can convert buoyancy-driven vertical momentum into horizontal momentum via the Coriolis terms. Without tilted rotation, this conversion can be achieved only by nonlinear mechanisms. The Coriolis forces thus tend to enhance mixing and the trend toward isotropy.

Enstrophy spectrum functions clarify at which scales this trend occurs. These functions Ω_H and Ω_V (from Cattaneo et al. 1991) are related to the vorticity components by

$$(\overline{\omega_x^2} + \overline{\omega_y^2})(z) = \int 2\Omega_H(k, z)dk , \qquad (22a)$$

$$\overline{\omega_z^2}(z) = \int \Omega_V(k, z)dk , \qquad (22b)$$

and exhibit the relative power residing in the vertical and horizontal components of enstrophy by wavenumber. Cattaneo et al. (1991) showed that nonrotating turbulent convection tended toward isotropy on the small scales, at least for the highest degrees of turbulence they could attain ($Re_\lambda \sim 20$; see their Fig. 10). Figure 10 here presents the same functions evaluated at midlayer and time-averaged for R0, the (higher resolution) equivalent of case 3 of Cattaneo et al. (1991), and for the moderately rotationally influenced case T1. Despite the lower supercriticality of T1 (by virtue
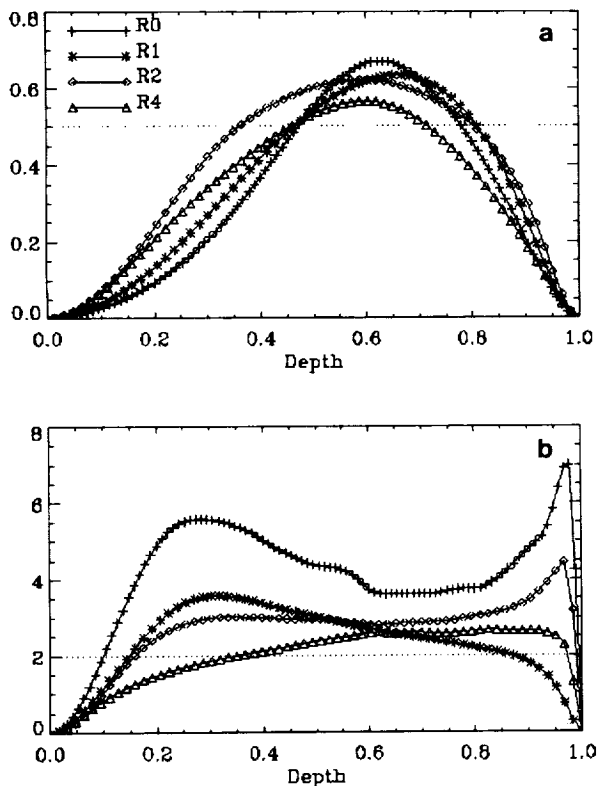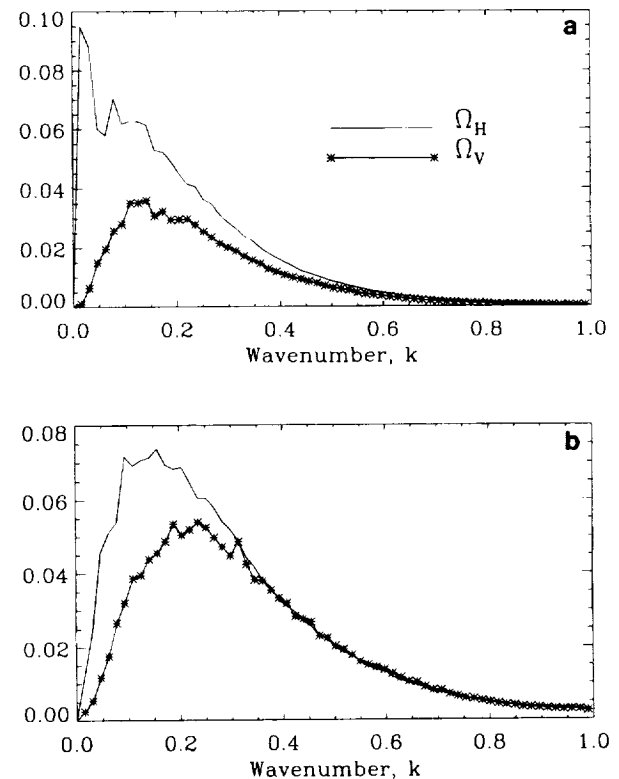

Fig. 9.—(a) Variation with depth of the ratio r_e of the kinetic energy in vertical motions to that in horizontal motions, horizontally and time averaged for the four simulations R0, R1, R2, and R4. (b) Companion ratio r_ω of the horizontal enstrophy to that in the vertical. With increasing rotational influence both ratios tend toward their isotropic values (dotted lines) of 0.5 and 2.0, respectively, in the interior of the layer.

Fig. 10.—Variation with wavenumber of the enstrophy spectrum functions Ω_H and Ω_V, measuring relative power in the horizontal and vertical components of enstrophy. Time-averaged spectra as evaluated at midlayer in (a) the nonrotating simulation R0 and (b) the moderately rotationally influenced simulation T1. The wavenumbers are normalized by the maximum resolved (i.e., dealiased) wavenumber. The overlapping curves at moderate to high wavenumbers in b indicates the isotropy at those scales, enhanced by the effects of rotation.

of the stabilizing rotation), the two curves Ω_H and Ω_V for T1 lie together for more than half the resolved wavenumbers whereas the R0 curves coincide only at the smallest scales. This indicates that, although the largest scales must still be dominated by the convective forcing, the effects of rotation enhance the isotropy on a wide range of scales from medium to small. Despite the increased presence of anisotropic coherent structures in tilted rotating convection, average measures such as these indicate that Coriolis forces mix the smaller scale components of momentum in the flow efficiently.

3.5. Rotational Alignment of Coherent Structures

Although effects of rotation due to vortex interactions tend to isotropize the interior turbulence on the smaller scales, the presence of rotation can simultaneously introduce anisotropy on the larger scales of motion, since coherent fluid trajectories may prefer a direction other than that dictated solely by buoyancy. If Coriolis forces are sufficiently strong and the rotation vector is not aligned with gravity, then buoyancy-driven fluid motions may be deflected during their vertical transit. The current simulations exhibit a distinct difference in the perturbation of fluid trajectories by Coriolis forces depending on whether the motions are laminar or turbulent. Laminar flows operate in cellular structures whose boundaries can tilt away from the vertical under the rotational influence. The smooth velocity trajectories within the cellular flow may also be perturbed by both components of the rotation. The strong effect of Ω_y on the vertical motions often dominates to leave streamlines which in general are not parallel to the rotation vector. Turbulent flows no longer exhibit smooth streamlines and distinct cellular boundaries but rather consist of small-scale motions punctuated by coherent structures. The effect of a rotational influence is then to align the large-scale vortical structures with the rotation vector. Laminar and turbulent flows thus exhibit streamline "tilting" or vortex structure "alignment," respectively. Any consistent perturbation of trajectories in the flow is of interest since a correlation between horizontal and vertical motions is thus generated. Such correlations provide Reynolds stresses, which are the only source terms for the generation of mean horizontal shear flows, and may also significantly affect the vertical heat flux since they reflect less direct communication between the horizontal boundaries. The presence of mean flows and the rotational influence on energy transport in the current context are discussed in subsequent papers in this series. In this paper, the structure of the convective flows that leads to such effects is addressed.

A clear exposé of the tilting of laminar fluid trajectories appears in linear stability calculations of f-plane Boussinesq convection by Hathaway, Gilman, & Toomre (1979) and Hathaway, Toomre, & Gilman (1980). Similar treatments of compressible convection are more complex since the onset is unsteady (Jones, Roberts, & Galloway 1990). The Boussinesq paper showed that, even in the absence of a thermal wind, the cellular boundaries of zonal (i.e., aligned along x) rolls tilt poleward, and upward (downward) motions veer to the west (east). In this linear stability analysis, the equivalent tilting of meridional rolls (aligned along y, the preferred mode at onset) in the zonal direction is suppressed by the pressure gradient in that direction. In later three-dimensional fully nonlinear but still laminar numerical simulations of the same type of rotating convection

(Hathaway & Somerville 1983), it was observed that the smooth flow trajectories and cellular structural boundaries could be significantly tilted both zonally and meridionally when mixed modes (zonal and meridional rolls) exist. This can be demonstrated by measuring a normalized global degree of correlation between velocity components $u_1, u_2, u_3 (=u, v, w)$,

$$\langle R_{i,j} \rangle_t = \left\langle \frac{\langle u_i u_j \rangle}{(\langle u_i^2 \rangle \langle u_j^2 \rangle)^{1/2}} \right\rangle_t , \qquad (23)$$

where unsubscripted angle brackets indicate an rms average over all space, and a t subscript indicates that this quantity is also time-averaged over many turnover times. Hathaway & Somerville (1983) reported a significant correlation $(R_{1,3} = -0.3)$ between upward and westward moving elements (uw correlations) for a case corresponding to $R_0 = 1$ at $\phi = 15°$ in their Boussinesq calculations. This correlation manifested itself as an obvious drift of the particle trajectories toward the west as they move upward and toward the east as they move downward. A correlation existed between upward and southward motions (vw correlation) as well but was a factor of 2 smaller ($R_{2,3} = -0.13$). In that case, the cellular flow is composed mainly of meridional rolls but the small zonal component tilts weakly poleward and generates particle paths which are strongly slanted in the zonal direction. A lower Rossby number solution exhibited much less correlation in both $R_{1,3}$ and $R_{2,3}$ since the conservation of angular momentum is lost due to significant pressure effects (Cowling 1951) in the now completely dominant meridional rolls.

Measures of the velocity correlations (23) for the cases under study here are included in Table 2. The laminar solutions L1–L3 exhibit lower values of the correlation than those from Hathaway & Somerville (1983), probably due to the larger $R_0 (= 2.29)$ and the lower P_r. However, as before the uw correlations are significantly larger than vw except when meridional rolls are prevalent (L3). Of greater importance, for turbulent solutions such as cases R3–R6 the velocity correlations are all reduced by at least a factor of 2. For moderately rotating turbulent cases (R1, R2, T1, T2), u correlates with w significantly better than v does. For a stronger rotational influence (such as simulations R4–R6), the values are either comparable or the uw correlations are smaller than those of vw, with the latter more dominant with increasing latitude. The general trends are toward a decorrelation of the flows with increasing turbulence as may be expected, with a decrease in the role of zonal-vertical (uw) correlations (and subsequent increase in the importance of meridional-vertical vw correlations) both with increasing rotational influence and with latitude. Figure 11 elucidates the reason for these changes in correlation in a typical turbulent case. It shows a volume rendering of a snapshot of enstrophy for case R4 which has strong rotational influence $(R_0 = 0.71)$ with the rotation vector lying at 45° to the horizontal in the $y - z$ plane. The only obvious correlation is a clear alignment of strong enstrophy structures along this direction. Laminar tilting of cellular boundaries and smooth streamlines has been replaced by rotational alignment of the coherent vortex structures in the flow.

This difference between the rotational influence on laminar and turbulent convective motions is clarified in the sketches of Figure 12. For laminar cases, where streamlines are smooth and the flow is cellular, tilting of cellular struc-

TABLE 2

TIME-AVERAGED GLOBAL VELOCITY CORRELATIONS $R_{i,j}$ AND VORTICITY ALIGNMENT

Case	$\left\langle \dfrac{\langle uw \rangle}{[\langle u^2 \rangle \langle w^2 \rangle]^{1/2}} \right\rangle_t$	$\left\langle \dfrac{\langle vw \rangle}{[\langle v^2 \rangle \langle w^2 \rangle]^{1/2}} \right\rangle_t$	$\left\langle \dfrac{\langle uv \rangle}{[\langle u^2 \rangle \langle v^2 \rangle]^{1/2}} \right\rangle_t$	$\left\langle \dfrac{\omega \cdot \Omega}{|\omega|} \right\rangle_t$
L1......	0.160	0.052	−0.112	0.592
L2......	0.026	0.008	0.041	0.611
L3......	0.040	0.116	−0.140	0.635
R0......	0.006	0.015	0.209	—
R1......	0.045	0.031	0.080	0.575
R2......	0.105	0.040	−0.013	0.586
R3......	0.083	−0.048	−0.069	0.590
R4......	−0.032	−0.041	−0.041	0.636
R5......	−0.111	0.097	−0.092	0.668
R6......	0.004	−0.061	0.012	0.645
T1......	0.105	−0.029	−0.081	0.583
T2......	0.131	0.011	−0.075	0.583

tures and fluid trajectories is forced by the action of the horizontal component of the rotation vector, Ω_y, on the space-filling, coherent vertical velocity field. Laminar motions which are not purely meridional rolls will have cellular boundaries tilted poleward with the rotation vector. However, an upward (downward) motion under the influence of Ω_y will be turned westward (eastward) providing a correlation between u and w. The fluid parcel paths are thus not parallel to the rotation vector. We term this effect *laminar tilting* of velocity trajectories and cellular structures. The vertical component of rotation, Ω_z, cannot affect vertical motions and serves only to transfer energy between the horizontal components of momentum, altering the horizontal particle trajectories somewhat within the cellular structure but not the geometry of the cell itself (Veronis 1959; Chandrasekhar 1961). On the other hand, when the solution is turbulent the small-scale isotropic motions of the interior turn over too quickly to sense the Coriolis force. The rotation acts solely on the *structures* within the flow

which have a significant coherence, aligning them in the direction of the rotation vector. We label this as *turbulent structural alignment*. Such alignment provides correlations between vertical and meridional motions since motions are parallel to the rotation vector on average along trajectories within the structure. Laminar and turbulent convective flows thus engender different correlations: laminar motions provide stronger uw correlations from the zonal tilting of trajectories, whereas turbulence creates vw coupling via particle paths within rotationally aligned structures.

Figure 13 isolates one typical tilted coherent structure in a turbulent flow. This figure shows particle streamlines where particles are advected by one snapshot of the velocity field as though it were a steady flow. The actual particle trajectories followed in time (streaklines) are somewhat more complicated due to inertial oscillations of the large-scale flows but are similar. A section $\frac{4}{3} : \frac{4}{3} : 1$ is extracted from the $4:4:1$ domain of the flow shown in Figure 11 that contains a coherent structure in enstrophy. Particle paths in the
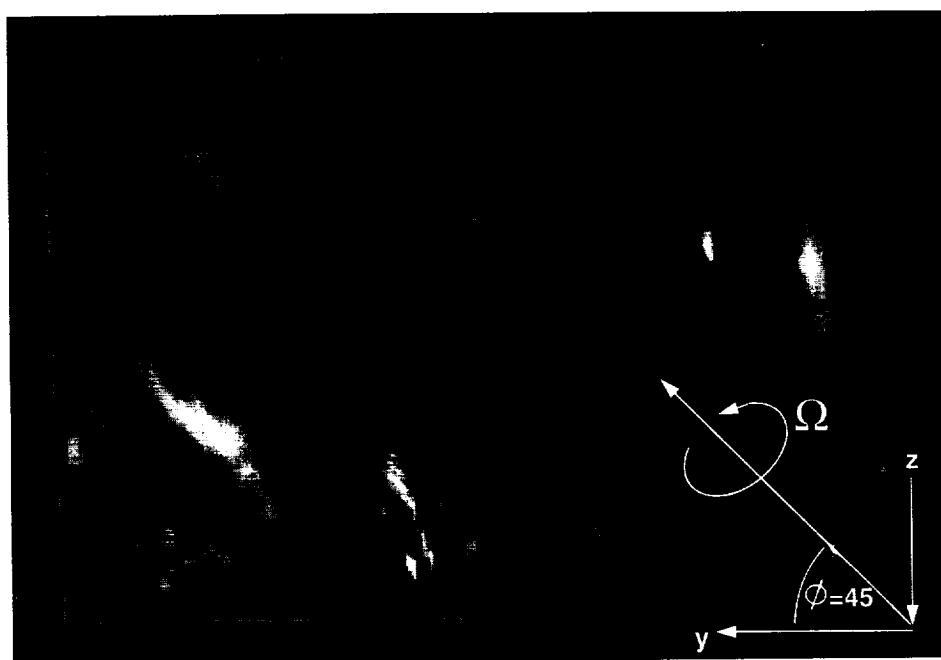

FIG. 11.—Volume rendering of enstrophy as viewed at one instant in time from the side of the layer in simulation R4. In such a strongly rotationally influenced case (with $R_0 = 0.71$), coherent vortex structures align with the rotation vector Ω over much of the layer.
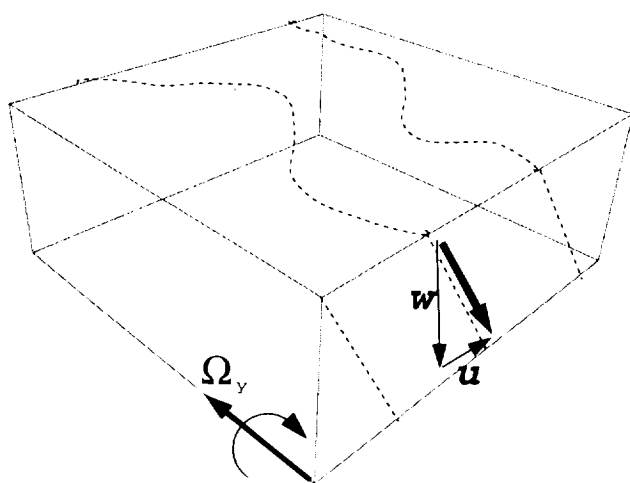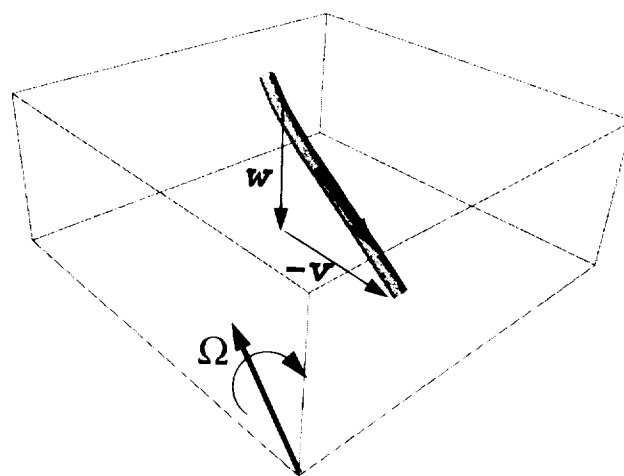
FIG. 12a

FIG. 12b

FIG. 12.—Sketches of the rotational influence on laminar and turbulent convective fluid trajectories. (a) In laminar cases, the horizontal component Ω_y of the rotation vector acting on the dominant buoyancy-driven vertical motions leads to tilting of the trajectories, yielding correlations between the u and w components of motion. These could serve to drive zonal mean flows. (b) In turbulent cases, coherent chimneys of strong vortical downflow become aligned with the tilted rotation vector, whereas the smaller scale motions are little influenced by Coriolis forces. The aligned structures possess correlations between the v and w components of motion which are sources for meridional mean flows.

structure clearly spiral parallel to the rotation axis. Such complexity here may be contrasted with the simple linear streamlines of the laminar Boussinesq flows in Hathaway & Somerville (1983). Laminar trajectories *are not* parallel to the rotation vector (although cell boundaries may be, for example in pure zonal rolls), whereas particle paths within structures in a turbulent flow *are* aligned with Ω (when averaged over the trajectory to remove the spiraling oscillations).

The new turbulent alignment of coherent structures appears to arise more as a natural consequence of the presence of a rotational direction among isotropic turbulent motions than as an action or instability of pre-existing vortex tubes in a rotating flow. Further work to clarify this is in progress (Brummell, Julien, & Rast 1996b). Figure 14 outlines a mechanism for the rotational alignment of fluid

parcels. The flow in general is driven by low entropy fluid leaving the upper boundary due to the effects of buoyancy. If the rotation vector is not aligned with gravity, then a vertical motion may be considered as the superposition of two orthogonal motions, one parallel to Ω and one perpendicular, say $w_\parallel$ and $w_\perp$, respectively. The former will experience no acceleration due to Coriolis forces, whereas the latter will feel a force which will tend to move a particle in an inertial circle in the plane perpendicular to the rotation vector. If $R_0 < 1$ then more than one inertial oscillation can be performed during the vertical transit and the sum of these two motions would be a spiral parallel to Ω.

Since this mechanism works on particle or parcel trajectories, the question is then to determine what distinguishes laminar flows from turbulent flows such that this mechanism is more obvious in the latter than the former. The answer to this is explored in detail in Brummell, Julien, &
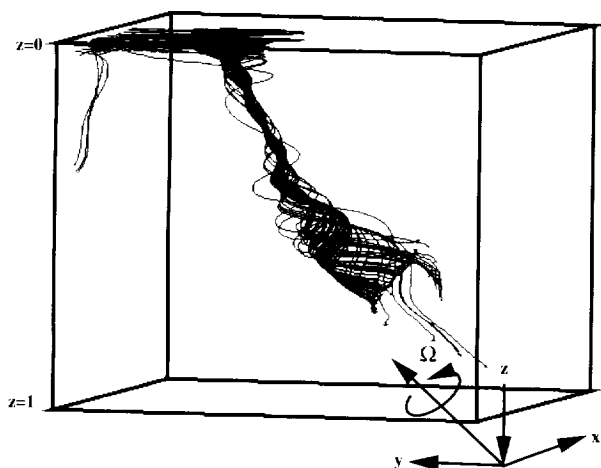

FIG. 13.—The helical winding of fluid trajectories is evident in a close-up view of a typical strong downflowing plume in a strongly rotating simulation R4. Shown are particle streamlines determined by advecting tracers with one snapshot of the velocity field as if it were a steady flow. The view encompasses the full depth of the layer, but only one-third of the extent in each of the horizontal directions.
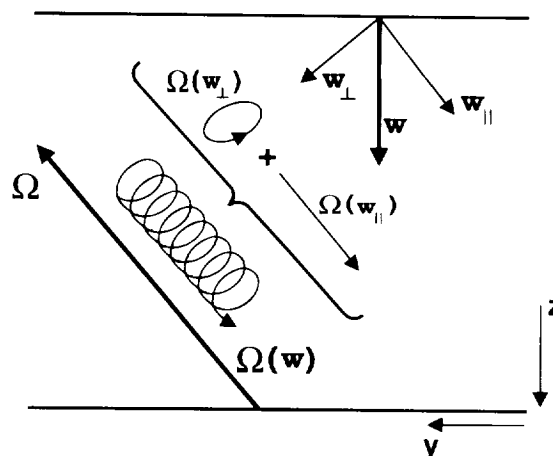

FIG. 14.—Sketch of the elements that contribute to the rotational alignment of turbulent convective motions with the rotation vector Ω. A buoyancy-driven vertical motion can be considered as the superposition of a component $w_\parallel$ parallel to the rotation vector and another $w_\perp$ perpendicular to it. The former experiences no Coriolis forces, whereas the latter is forced to move in inertial circles, the composite of which is a spiraling flow parallel to the rotation vector.

Rast (1996) and is explained only briefly here. Consider solely the effect of Coriolis forces in the momentum equations (3b),

$$\partial_t \rho u \sim \rho v \Omega_z - \rho w \Omega_y \,, \qquad (24a)$$

$$\partial_t \rho v \sim -\rho u \Omega_z \,, \qquad (24b)$$

$$\partial_t \rho w \sim \rho u \Omega_y \,. \qquad (24c)$$

These equations represent inertial oscillations about each of the rotation vector components, which transfer momentum between ρu and ρw via Ω_y and between ρu and ρv through Ω_z. If Ω_y and Ω_z are of the same order of magnitude, then the balance of these terms depends upon the magnitude of the momentum components themselves. If the vertical component ρw is originally the dominant entity, then the Coriolis force produces ρu via the horizontal component of the rotation, Ω_y. The zonal momentum produced feeds back into the vertical momentum via the inertial oscillation and only produces meridional momentum ρv at this secondary stage. If pressure effects are not significant, the transfer between u and w will probably be the strongest, corresponding to zonal tilting. On the other hand, if the horizontal components of momentum are initially of the same order of magnitude as the vertical component, then there is strong interaction with both components of the rotation vector leading to dual inertial oscillations. This creates an oscillation in the plane perpendicular to Ω, equivalent to an alignment of vorticity in that direction. Laminar flows are driven vertically by buoyancy and dominantly producing horizontal vorticity, with little transfer to vertical vorticity since the nonlinear advection terms are weak. In turbulent flows, however, there is a strong nonlinear production of vertical vorticity from the buoyant horizontal vorticity leading to an equipartition in strength between all three components of momentum. Thus the vertically dominated motions of laminar convection will most likely engender tilting of the smooth trajectories, whereas turbulent flows will tend to produce aligned vortical fluid from motions that have coherence on the order of the rotation time.

If the components of the rotation vector are not of the same order of magnitude, as is the case for a tilted rotation vector near the pole or the equator, then one of the two mechanisms becomes enhanced. Near the pole, Ω_y becomes unimportant, inertial oscillations about Ω_z dominate, and turbulent alignment and buoyancy act together. Near the equator, the turbulent alignment is in competition with buoyancy and Ω_y is dominant, so that tilting of coherent flows may be more likely. Since turbulent motions still possess large-scale overturnings with the small-scale turbulent motions superimposed, the resulting correlations for turbulent solutions stem from a balance of the two mechanisms.

3.6. Measures of Turbulent Structural Alignment

Inertial helical oscillations interfere with any instantaneous measurement or visualization of the velocity correlations. Only averaging over a full fluid trajectory will reveal the underlying correlation. This suggests that for turbulent alignment the velocity correlations may not be the optimal quantities to examine. Since the enstrophy data reveals such alignment more clearly, an attempt to quantify the correlation in terms of vorticity might be more fruitful. A measure of the degree of vorticity alignment with the unit

rotation vector $\hat{\Omega}$ is defined as

$$\omega_\Omega = \frac{\omega \cdot \hat{\Omega}}{|\omega|} \,. \qquad (25)$$

If the vorticity at a point is aligned along the rotational axis, then this quantity yields unity if the vorticity is cyclonic (and -1 if it is aligned but anticyclonic). If the vorticity is normal to the rotational vector at a point, then the value of ω_Ω there is zero. Note that a random vector field will register an average value of

$$\langle \omega_\Omega \rangle = \frac{1/3}{[(1/3)^2 + (1/3)^2 + (1/3)^2]^{1/2}} = \frac{1}{\sqrt{3}} \simeq 0.577 \,, \qquad (26)$$

since all directions are equally likely. Table 2 includes a listing of the rms spatial average of this quantity also averaged over many turnover times in each simulation, $\langle \omega_\Omega \rangle_t$. Although there is a trend toward more alignment with increasing influence of rotation, the variations from the value for a randomly orientated vector field are remarkably small. For cases R1–R4 where R_0 is decreasing, the value of $\langle \omega_\Omega \rangle_t$ increases from 0.575 to 0.636. Cases that are highly turbulent but moderately rotationally influenced, such as T1, remain marginally above the random value. Less turbulent cases with moderate rotation can have a reasonably high value of vorticity alignment, especially where the latitude is low, as in case L3. This reflects an alignment of laminar rolls along the dominant component of the rotation, Ω_y.

Despite the strong visual alignment for cases such as R4 (Fig. 11), $\langle \omega_\Omega \rangle_t$ is still close to the random value, varying by only 10% or so. This reflects the weak influence of the rotation for turbulent cases. Overall, the flow becomes largely decorrelated with only small regions of high correlation whose filling factor are not significant enough to influence a global measure significantly. Despite the small degree of alignment indicated in such measures, they at least appear to exhibit the expected direction. Figure 15a presents a plot of $\omega_\Omega(\phi_i)$ (rms-averaged over space) which is a measure of the degree of alignment with an arbitrary unit vector defined in the plane $y - z$ pointed at angle ϕ_i. The figure shows this measure for various ϕ_i between 0° and 90° for two cases, one with strong rotation (R4) and the other with moderate (T1), both positioned at latitude $\phi = 45°$ on the sphere. If the flow were to be aligned with the true rotation vector, then this measure should peak at the latitudinal inclination of that actual rotation vector, shown as the dotted line. A typical time from the less rotationally constrained case T1 can be seen to have a peak alignment with a horizontal unit vector ($\phi_i = 0°$). This indicates little alignment with the rotation, with the directionality being mainly influenced by the horizontally orientated vorticity generated by the convective overturning. On the other hand, a typical snapshot from the strongly rotationally constrained case R4 shows a peak alignment with a direction slightly more vertical than the actual rotation vector. This is an indication of considerable rotational alignment, with the error being forced by two mechanisms. First, convective overturning tends to align structures vertically by the action of buoyancy parallel to gravity. Second, the boundary conditions influence the flows. Since the boundaries are stress free, only vertical vorticity can exist there, and thus vortex structures are forced to be aligned vertically near the
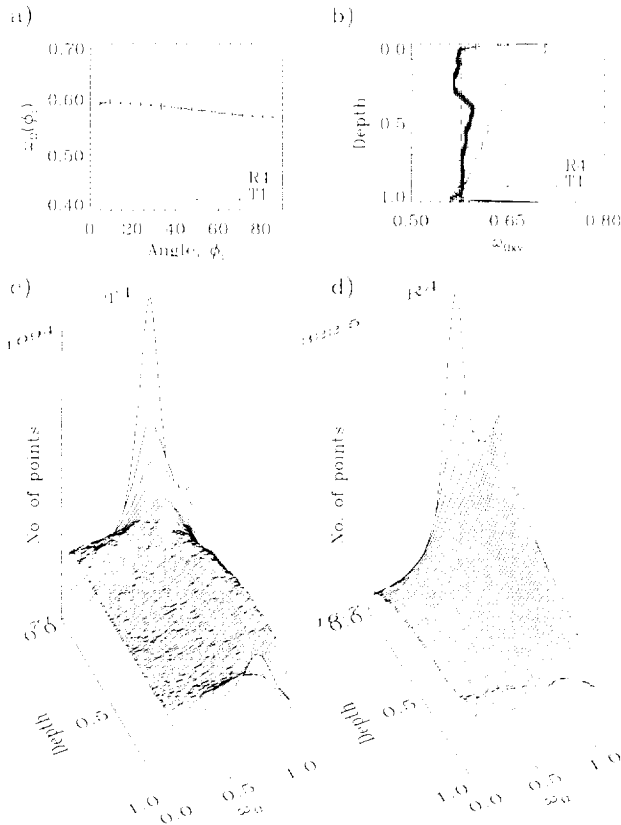
FIG. 15.—Average and pointwise measures of vorticity alignment within the strongly rotationally constrained case R4 and the moderately constrained case T1. (a) A measure $\omega_\Omega(\phi_i)$ of the alignment of vorticity along an arbitrary direction specified by the angle ϕ_i in the $y-z$ plane, shown as ϕ_i is varied. Values are rms averaged over the full domain at a typical time. Panel (b) shows $\omega_{\Omega_{xy}}$, the alignment of vorticity with the actual rotation vector ω_Ω averaged over horizontal planes, plotted against depth for one typical snapshot in time. Panels (c) and (d) show histograms of the pointwise measure ω_Ω at each depth, averaged over many turnover times in simulations T1 and R4, respectively.

boundaries, an influence which will show up in the global measure $\langle \omega_\Omega \rangle$.

To isolate the alignment more clearly, the remaining panels of Figure 15 exhibit plane-average and pointwise statistics. Figure 15b shows the breakdown of the global rms measure $\langle \omega_\Omega \rangle$ into rms values calculated at each depth, $\omega_{\Omega_{xy}} = \langle \omega_\Omega \rangle_{xy,\mathrm{rms}}(z)$, for the same two typical cases from R4 and T1. The higher R_0 case T1 shows the measure to hover around the equipartition value (0.577, shown as the dashed line) for the majority of the interior, with a jump to the value representing vertical alignment at the boundaries (equal to sin ϕ, shown as the dotted line). The lower R_0 case R4 is also forced to have the same boundary values but shows a considerably higher degree of alignment throughout the box at each depth, with the measure only dropping toward the equipartition value near the lower boundary. However, this horizontally averaged measure never exhibits a stronger alignment anywhere in the flow than that at the boundaries where structures are forced to be completely misaligned. This is again a reflection of the small filling factor of the aligned structures in a sizable average, a problem which can only be resolved by examining pointwise measures.

Figures 15c–15d show (time-averaged) histograms of the earlier measure ω_Ω evaluated over horizontal planes at each

depth and then stacked, for the two cases previously considered. At any depth, a peak in the histogram at any value of ω_Ω indicates that a large number of points are aligned to that degree. For example, in both cases, the histograms at the boundaries show a strong peak at $\omega_\Omega = \sin(\pi/4)$. This corresponds once again to the forced vertical alignment mismatch with the 45° rotation vector. However, away from the boundaries, the histograms in Figure 15c for case T1 show a flat profile indicating that there are as many points aligned in one direction as in any other. Figure 15d for the strong rotation case R4, however, reveals that away from the boundaries the histogram peaks at the value of $\omega_\Omega = 1$. More points are indeed aligned with the rotational vector at each depth than any other direction. However, this is not a sharp peak, and thus there are still a large number of points aligned in other directions which will mask any average statistics.

To calculate the filling factor of aligned structures explicitly, the fraction of the area at any depth that is covered by points with greater than a certain degree of alignment may be measured by the quantity

$$p(\omega_\Omega^0) = \frac{N_>}{N_{\mathrm{tot}}}, \qquad (27)$$

where $N_>$ is the number of points with $\omega_\Omega > \omega_\Omega^0$ and N_{tot} is the total number of points in any horizontal plane. For the higher R_0 case, T1, $p(0.9)$ attains a maximum value of 0.11 at depth $z = 0.59$ (although this fraction is relatively constant throughout the interior). For the lower R_0 case R4 this maximum value is 0.2 at $z = 0.12$ (and decreases throughout the interior). This implies that the most strongly aligned Fluid (top 10%) is contained in 11% of the area in case T1 and in 20% in case R4. The value of $z = 0.12$ for R4 corresponds roughly to the edge of the thermal boundary layer. This depth may be that at which the vertically aligning influence of the boundary is no longer felt, and yet the coherence of the strong downflowing structures is still evident so that the rotation may act easily on such tubes. Once in the interior, although such structures remain somewhat coherent across the entire layer depth, they are eroded by the shear and buffeted by the turbulent motions, so that their alignment is diminished. The filling factor for these structures, however, is always small even when strong rotation is present. However, these changes in the nature of the turbulent rotating solutions have profound consequences for the mean flows that coexist with the convection, as shall be seen in Paper II.

Although it is quite difficult to quantify the properties of such multiscale rotating turbulence, the general impressions are quite clear. The convection involves small-scale turbulent motions that are isotropic, decorrelated, and influenced only indirectly by rotation. Punctuating and coexisting with these motions are distinctly anisotropic, extended (but volumetrically small) structures of considerable coherence that sense and align with strong rotation significantly.

4. CONCLUSIONS

Compressible convection in a simple rectilinear domain influenced by a constant magnitude rotation has been studied. The angle between the rotation vector and gravity is not necessarily zero mimicking the placement of the domain at various latitudes on a sphere. The thermal forcing extends to regimes where motions are turbulent.

This paper addresses the changes in structure and evolution of the convective flow associated with the variation of the rotational influence, as measured by the convective Rossby number R_0.

The underlying structure of the turbulent rotating convection remains similar to that of nonrotating simulations (e.g., Cattaneo et al. 1991). The flows are divided into an upper thermal boundary layer consisting of a laminar, cellular network, atop a fully turbulent interior punctuated by vertically coherent structures emanating from the upper surface. However, the inclusion of rotation changes the characteristics of both the surface network and the turbulent interior. The surface network becomes more curvaceous, less connected, and more time dependent under the rotational influence. The overall mobility of the cellular pattern is due to inertial motions of the surface flows induced by the Coriolis forces. Rotational enhancement of a dynamical buoyancy mechanism operating at the junctions of the network leads to self-destruction of these interstices and thus a new method of cell creation.

The turbulent interior of the flow is also subtly altered in nature. The components of the rotation vector provide a linear mechanism for transferring momentum between vertical and horizontal motions. In contrast, for nonrotating convection, the only method of exchange is through the nonlinear advective terms of the equations. Hence it is not surprising that with rotation the isotropy of energy and enstrophy is enhanced. This manifests itself as the concentration of vorticity into more distinct tube-like structures with a very random orientation in the interior of the flow. The interactions of vortex tubes on various scales provide a horizontal mixing mechanism for the thermodynamic properties. Vertical velocity and thermal fluctuations become less correlated in the interactions, retarding the efficiency of the vertical convective transport and consequently leaving a superadiabatic mean stratification in the interior. Motions in the turbulence may now be thermally driven at any depth, not just in the thermal boundary layers.

While increasing the mixing of momentum toward isotropy on the small scales of motion in the turbulent cases, strong rotation can also induce an anisotropy on the large scales by introducing a preferred direction. The coherent structures of the turbulent flows have a tendency to align with the rotation vector under the action of the Coriolis force. This mechanism is distinctly different from that found in laminar flows, where the fluid trajectories of the large-scale overturning are subject to a zonal tilting provided by the horizontal component of the rotation. The enhanced role of Ω_y in the laminar flows results from the dominance of buoyancy-driven horizontal vorticity over vertical. Turbulent cases have sufficient nonlinearity to equipartition energy between all of the three directions, and thus the motions sense all components of rotation. When all components of momentum are equally strong, the natural form of motion is helical and parallel to the rotation. These laminar and turbulent mechanisms provide disparate velocity correlations. The former provides a coupling between zonal and vertical motions, whereas turbulent convection generally becomes decorrelated but with a bias toward the coupling of meridional flows with vertical motions in the coherent structures.

For turbulent rotating convection, the global degree of correlation is reduced compared to the laminar cases (a signature of the turbulence) and is difficult to measure because of the low filling factor and time dependence of the coherent structures. However, much attention has been paid here to these laminar tilting and turbulent alignment mechanisms within the flows examined because they can lead to the generation of specific Reynolds stresses in the flow, which in turn are sources for large-scale (mean) flows. Indeed, in these simulations, such horizontally averaged flows are stable and significant and exhibit many interesting properties which may provide insight into the nature of the differential rotation of stars like the Sun. The mechanism for such inverse cascades to large-scale mean shearing flows is the subject of Paper II.

REFERENCES

Arendt, S. 1993, ApJ, 412, 664
Baker, L., & Spiegel, E. A. 1975, J. Atmos. Sci., 32, 1909
Bogdan, T. J., Cattaneo, F., & Malagoli, A. 1994, ApJ, 407, 316
Brandenburg, A., Jennings, R. L., Nordlund, A., Rieutord, R., Stein, R. F., & Tuominen I. 1995, J. Fluid Mech., submitted
Brown, T. M., Christensen-Dalsgaard, J., Dziembowski, W. A., Goode, P. R., Gough, D. O., & Morrow, C. A. 1989, ApJ, 242, 526
Brown, T. M., & Morrow, C. A. 1987, ApJ, 314, L21
Brummell, N. H., Cattaneo, F., Malagoli, A., Toomre, J., & Hurlburt, N. E. 1991, in Lecture Notes in Physics, 88, Challenges to Theories of the Structure of Moderate-Mass Stars, ed. D. O. Gough & J. Toomre (Berlin: Springer), 189
Brummell, N. H., Cattaneo, F., & Toomre, J. 1995, Science, 269, 1313
Brummell, N. H., Hurlburt, N. E., & Toomre, J. 1996, in preparation (Paper II)
Brummell, N. H., Julien, K. A., & Rast, M. P. 1996, in preparation
Busse, F. H. 1970, ApJ, 159, 629
Busse F. H., & Cuong P. G. 1977, Geophys. Astrophys. Fluid Dyn., 8, 17
Canuto, C., Hussaini, M. Y., Quarteroni, A., & Zang, T. A. 1988, Spectral Methods in Fluid Dynamics (New York: Springer)

Castaing, B., et al. 1989, J. Fluid Mech., 204, 1
Cattaneo, F., Brummell, N. H., Toomre, J., Malagoli, A., & Hurlburt, N. E. 1991, ApJ 370, 282
Cattaneo, F., Hurlburt, N. E., & Toomre, J. 1989, in Stellar and Solar Granulation, ed. R. J. Rutten & G. Severino (Dordrecht: Kluwer), 415
————. 1990, ApJ, 349, L63
Chan, K. L., & Sofia, S. 1986, ApJ, 307, 222
————. 1987, Science, 235, 465
Chandrasekhar, S. 1961, Hydrodnamic and Hydromagnetic Stability (Oxford: Clarendon)
Cowling, T. G. 1951 ApJ, 114, 272.
DeLuca, E. E., Werne, J., Rosner, R., & Cattaneo, F. 1990, Phys. Rev. Lett., 64, 2370
Durney, B. R. 1987, in The Internal Solar Angular Velocity, ed. B. R. Durney & S. Sofia (Dordrecht: Reidel), 235
Edwards, J. M. 1990, MNRAS, 242, 224
Gilman P. A. 1975, J. Atmos. Sci., 32, 1331
————. 1977, Geophys. Astrophys. Fluid Dyn., 8, 93
Gilman, P. A., & Glatzmaier, G. A. 1981, ApJS, 45, 351
Gilman, P. A., & Miller, J. 1986, ApJS, 61, 585

Glatzmaier, G. A. 1984, J. Comput. Phys., 55, 461
———. 1985, ApJ, 291, 300
———. 1987, in The Internal Solar Angular Velocity, ed. B. R. Durney & S. Sofia (Dordrecht: Reidel), 263
Glatzmaier, G. A., & Gilman, P. A. 1981, ApJS, 45, 335
Glatzmaier, G. A., & Toomre, J. 1995, in ASP Conf. Ser., Vol. 76, GONG '94: Helio- and Astero-Seismology from the Earth and Space, ed. R. K. Ulrich, E. J. Rhodes, Jr., & W. Däppen (San Francisco: ASP), 200
Gough, D. O., Moore, D. R., Spiegel, E. A., & Weiss, N. O. 1976, ApJ, 206, 536
Gough D. O., & Toomre J. 1991, ARA&A, 29, 627
Gough, D. O., & Weiss, N. O. 1976, MNRAS, 176, 589
Graham, E. 1975, J. Fluid Mech., 70, 689
———. 1977, in IAU Colloq. 38, Problems of Stellar Convection, ed. E. A. Spiegel & J.-P. Zahn (Berlin: Springer), 151
Harvey, J., & The GONG Instrument Team. 1995, in ASP Conf. Ser., Vol. 76, GONG '94: Helio- and Astero-Seismology from the Earth and Space, ed. R. K. Ulrich, E. J. Rhodes, Jr., & W. Däppen (San Francisco: ASP), 432
Hathaway, D. H. 1984, ApJ, 276, 316
Hathaway, D. H., Gilman P. A., & Toomre J. 1979, Geophys. Astrophys. Fluid Dyn., 13, 289.
Hathaway, D. H., & Somerville, R. C. J. 1983, J. Fluid Mech., 126, 75
———. 1986, J. Fluid Mech., 164, 91
———. 1987, Geophys. Astrophys. Fluid Dyn., 38, 43
Hathaway, D. H., Toomre, J., & Gilman P. A. 1980, Geophys. Astrophys. Fluid Dyn., 15, 7
Heslot, F., Castaing, B., & Libchaber, A. 1987, Phys. Rev. A, 36, 5870
Hossain, M., & Mullan, D. J. 1990, ApJ, 354, L33
Hurlburt, N. E., Brummell, N. H., & Toomre, J. 1995, in Proc. 4th SOHO Workshop Helioseismology, ed. J. T. Hoeksema et al. (Noorwijk: ESA), ESA SP-376, 2, 245
Hurlburt, N. E., Toomre, J., & Massaguer, J. M. 1984, ApJ, 282, 557
Hurlburt, N. E., Toomre, J., & Massaguer, J. M. 1986, ApJ, 311, 563
Hurlburt, N. E., Toomre, J., Massaguer, J. M., & Zahn, J.-P. 1994, ApJ, 421, 245
Jones, C. A., Roberts, P. H., & Galloway, D. J. 1990, Geophys. Astrophys. Fluid Dyn., 53, 145
Julien, K., Legg, S., McWilliams, J., & Werne, J. 1996, J. Fluid Mech., 322, 243
Korzennik, S. G., Rhodes, E. J., Jr., Johnson, N. M., Rose, P., & Cacciani, A. 1995, in ASP Conf. Ser., 76, GONG '94: Helio- and Astero-Seismology from the Earth and Space, ed. R. K. Ulrich, E. J. Rhodes, Jr., & W. Däppen (San Francisco: ASP), 12
Latour, J., Toomre, J., & Zahn, J.-P. 1981, ApJ, 248, 1081
Libbrecht, K. G. 1989, ApJ, 336, 1092
Malagoli, A., Cattaneo, F., & Brummell, N. H. 1990, ApJ, 361, L33
Massaguer, J. M., Latour, J., Toomre, J., & Zahn, J.-P. 1984, A&A, 140, 1
Nordlund, Å. 1982, A&A, 107, 1
———. 1983, in IAU Symp., 102, Solar and Stellar Magnetic Fields: Origins and Coronal Effects, ed. J. O. Stenflo (Dordrecht: Reidel), 79
Nordlund, Å. 1984, in The Hydromagnetics of the Sun, ed. G. A. Guyenne (Noordwijk: ESA), ESA SP-220, 37
Nordlund, Å. 1985, in Theoretical Problems in High Resolution Solar Physics, ed. H. U. Schmitt (Munich: Max-Plank-Institute für Astrophysik), 1

Nordlund, Å., & Stein, R. F. 1990, Comput. Phys. Comm., 59, 119
———. 1991, in Lecture Notes Phys., Vol. 388, Challenges to Theories of Moderate-Mass Stars, ed. D. O. Gough & J. Toomre (Berlin: Springer), 141
Parker, E. N. 1991, ApJ, 380, 251
Pedlosky, J. 1979, Geophysical Fluid Dynamics (Berlin: Springer)
Porter, D. H., & Woodward, P. R. 1994, ApJS, 93, 309
———. 1996, in preparation
Porter, D. H., Woodward, P. R., Yang, W., & Mei, Q. 1990, in Ann. NY Acad. Sci., Vol. 617, Nonlinear Astrophysical Fluid Dynamics, ed. R. Buchler (New York: New York Acad. Sci.), 234
Pouquet, A., Porter, D. H., & Woodward, P. 1994, Phys. Fluids, 6, 2133
Proudman, J. 1916, Proc. R. Soc. Lond. A, 92, 408
Pulkinnen, P. Tuominen, I., Brandenburg, A., Nordlund, Å., & Stein, R. F. 1993, A&A, 267, 265
Rast, M. P. 1996, in preparation
Rast, M. P., Nordlund, Å., Stein, R. F., & Toomre, J. 1993, ApJ, 408, L53
Rast, M. P., & Toomre, J. 1993a, ApJ, 419, 224
———. 1993b, ApJ, 419, 240
Richtmyer, R. D., & Morton, K. W. 1967, Difference Methods for Initial Value Problems (New York: Interscience)
Rosner, R., & Weiss, N. O. 1985, Nature, 317, 790
Rüdiger, G. 1989, Differential Rotation and Stellar Convection: Sun and Solar-type Stars (New York: Gordon & Breach)
Scherrer, P. H., et al. 1995, Sol. Phys., 162, 129
She, Z.-S., Jackson E., & Orszag S. 1990, Nature, 344, 226
Sofia, S., & Chan, K. L. 1984, ApJ, 282, 550
Somerville, R. C. J., & Lipps, F. R. 1973, J. Atmos. Sci., 30, 590.
Stein, R., & Nordlund, Å. 1989, ApJ, 342, L95
Stein, R. F., & Nordlund, A. 1991, in Lecture Notes Phys., 388, Challenges to Theories of Moderate-Mass Stars, ed. D. O. Gough & J. Toomre (Berlin: Springer), 195
———. 1994, in IAU Symp. 154, Infrared Solar Physics, ed. D. Rabin, J. Jeffries & C. Lindsey (Dordrecht: Kluwer), 225
Stein, R., Nordlund, Å., & Kuhn, J. R. 1989, in Stellar and Solar Granulation, ed. R. J. Rutten, & G. Severino (Dordrecht: Kluwer), 381
Taylor, G. I. 1921, Proc. R. Soc. Lond. A, 100, 114
Tomczyk, S., Schou, J., & Thompson, M. J. 1995, ApJ, 448, L57
Toomre, J., & Brummell, N. H. 1995, in Proc. 4th SOHO Workshop Helioseismology, ed. J. T. Hoeksema et al. (Noorwijk: ESA), ESA SP-376, 1, 47
Toomre, J., Brummell, N. H., Cattaneo, F., & Hurlburt, N. E. 1990, Comput. Phys. Comm., 59, 105
Veronis, G. 1959, J. Fluid Mech., 5, 401
Vincent, A., & Meneguzzi, M. 1991, J. Fluid Mech., 225, 1
Werne, J. 1993, Phys. Rev. E., 48, 1020
Werne, J., DeLuca, E. E., Rosner, R., & Cattaneo, F. 1991, Phys. Rev. Lett., 67, 3519
Woodward, P. R., Porter, D. H., Winkler, K.-H., Chalmers, J. W. Hodson, S. W., & Zabusky, N. J. 1987, in Science and Engineering on Cray Supercomputers (Minneapolis: Cray Res.), 557